

T-bet⁺CD8⁺ T cells govern anti-PD-1 responses in microsatellite-stable gastric cancers

Received: 25 April 2024

Accepted: 4 April 2025

Published online: 25 April 2025



Shiying Tang^{1,2,3,4,9}, Xiaofang Che^{1,2,3,4,9}, Jinyan Wang⁵, Ce Li^{1,2,3,4}, Xin He^{1,2,3,4}, Kezuo Hou^{1,2,3,4}, Xiaojie Zhang^{1,2,3,4}, Jia Guo^{1,2,3,4}, Bowen Yang^{1,2,3,4}, Danni Li^{1,2,3,4}, Lili Cao^{1,2,3,4}, Xiujuan Qu^{1,2,3,4,10}✉, Zhenning Wang^{6,7,8,10}✉ & Yunpeng Liu^{1,2,3,4,10}✉

More than 90% of advanced gastric cancers (GC) are microsatellite-stable (MSS). Compared to the high response rate of immune checkpoint inhibitors (ICI) in microsatellite-instability-high (MSI-H) GCs, only 10% of unstratified MSS GCs respond to ICIs. In this study, we apply semi-supervised learning to stratify potential ICI responders in MSS GCs, achieving high accuracy, quantified by an area under the curve of 0.924. Spatial analysis of the tumor microenvironment of ICI-sensitive GCs reveals a high level of T-bet⁺ CD8⁺ T cell infiltration in their tumor compartments. T-bet⁺ CD8⁺ T cells exhibit superior anti-tumor activity due to their increased ability to infiltrate tumors and secrete cytotoxic molecules. Adoptive transfer of T-bet⁺ CD8⁺ T cells boosts anti-tumor immunity and confers susceptibility to ICIs in immune-ignorant MSS GCs in a humanized mouse model. Spatial RNA sequencing suggests a positive-feedback loop between T-bet⁺ T cells and PD-L1⁺ tumor cells, which eventually drives T cell exhaustion and can therefore be leveraged for ICI therapy. In summary, our research provides insights into the underlying mechanism of anti-tumor immunity and deepens our understanding of varied ICI responses in MSS GCs.

Gastric cancer (GC) is one of the leading causes of cancer-related death globally¹. Cytotoxic chemotherapies remain the first-line treatment for most advanced GCs; however, the median overall survival (OS) fails to exceed one year^{2–5}. Immune checkpoint inhibitors (ICIs, e.g., PD-1/PD-L1 inhibitors) have shown great promise in multiple solid tumors^{6,7}. In GCs,

PD-1 inhibitors have demonstrated a superior anti-tumor activity in Microsatellite instability-high/deficient mismatch repair (MSI-H/dMMR) cancers, with the overall response rates (ORRs) ranging from 45% to 60%, comparing to 10% ORRs in microsatellite-stable/proficient mismatch repair (MSS/pMMR) GCs^{8–12}. The rationale for a higher response rate in

¹Department of Medical Oncology, The First Hospital of China Medical University, No. 155, Nanjing Street, Shenyang, Liaoning, China. ²Key Laboratory of Anticancer Drugs and Biotherapy of Liaoning Province, The First Hospital of China Medical University, Shenyang, Liaoning, China. ³Clinical Cancer Research Center of Shenyang, the First Hospital of China Medical University, Shenyang, China. ⁴Key Laboratory of Precision Diagnosis and Treatment of Gastrointestinal Tumours, Ministry of Education, Shenyang, Liaoning, China. ⁵Department of Immunology, College of Basic Medical Sciences, China Medical University, No. 77, Puhe Road, Shenyang, Liaoning, China. ⁶Department of Surgical Oncology and General Surgery, The First Hospital of China Medical University, No.155, Nanjing Street, Shenyang, Liaoning, China. ⁷Key Laboratory of Precision Diagnosis and Treatment of Gastrointestinal Tumours, Ministry of Education, China Medical University, Shenyang, Liaoning, China. ⁸Institute of Health Sciences, China Medical University, Shenyang, Liaoning, China. ⁹These authors contributed equally: Shiying Tang, Xiaofang Che. ¹⁰These authors jointly supervised this work: Xiujuan Qu, Zhenning Wang, Yunpeng Liu. ✉e-mail: xjq@cmu.edu.cn; znwang@cmu.edu.cn; ypliu@cmu.edu.cn

Table 1 | Clinical characteristics of patients in GC-ICI cohort

Patient ID	MSI	EBV	Subtype	Treatment	BOR	Response	Progression	PFS (days)
ICI-1	+	-	MSI-H	Anti-PD-1	PR	1	0	218
ICI-2	-	+	EBV(+) MSS	Anti-PD-1 + Apatinib	SD	0	0	85
ICI-3	-	-	EBV(-) MSS	Anti-PD-1 + Oxaliplatin	SD	0	0	55
ICI-4	-	-	EBV(-) MSS	Anti-PD-1 + Apatinib	PD	0	1	28
ICI-5	-	-	EBV(-) MSS	Anti-PD-1 + Apatinib	PD	0	1	30
ICI-6	-	-	EBV(-) MSS	Anti-PD-1 + S-1 + Oxaliplatin	SD	0	0	145
ICI-7	+	-	MSI-H	Anti-PD-1	SD	0	0	53
ICI-8	-	+	EBV(+) MSS	Anti-PD-1 + Oxaliplatin + Capecitabine	PR	1	1	332
ICI-9	-	-	EBV(-) MSS	Anti-PD-1 + Paclitaxel	PR	1	1	215
ICI-10	+	-	MSI-H	Anti-PD-1	PR	1	0	328
ICI-11	-	-	EBV(-) MSS	Anti-PD-1 + Irinotecan	SD	0	0	125
ICI-12	+	-	MSI-H	Anti-PD-1	PR	1	0	130
ICI-13	+	-	MSI-H	Anti-PD-1	SD	0	1	222
ICI-14	-	-	EBV(-) MSS	Anti-PD-1 + S-1 + Oxaliplatin	SD	0	0	72
ICI-15	+	-	MSI-H	Anti-PD-1	PR	1	1	265
ICI-16	-	+	EBV(+) MSS	Anti-PD-1	SD	0	1	281
ICI-17	-	-	EBV(-) MSS	Anti-PD-1 + S-1 + Oxaliplatin	SD	0	0	47
ICI-18	-	-	EBV(-) MSS	Anti-PD-1 + Paclitaxel + Apatinib	SD	0	0	139
ICI-19	-	-	EBV(-) MSS	Anti-PD-1	PR	1	0	90
ICI-20	-	-	EBV(-) MSS	Anti-PD-1 + Paclitaxel + Apatinib	SD	0	0	80
ICI-21	-	-	EBV(-) MSS	Anti-PD-1 + S-1 + Paclitaxel	SD	0	0	111
ICI-22	-	+	EBV(+) MSS	Anti-PD-1 + Irinotecan	SD	0	1	137
ICI-23	-	-	EBV(-) MSS	Anti-PD-1 + Paclitaxel	PD	0	1	44
ICI-24	-	-	EBV(-) MSS	Anti-PD-1 + Irinotecan	SD	0	1	94
ICI-25	+	-	MSI-H	Anti-PD-1 + Paclitaxel + Cisplatin	SD	0	0	66

Responses are evaluated using RECIST 1.1. *MSI* microsatellite instability, *EBV* Epstein–Barr virus, *BOR* best of response, *PFS* progression free survival, *PR* partial response, *SD* stable disease, *PD* progressed disease. 1 stands for positive; 0 stands for negative.

MSI-H GCs is that these tumors harbor a significant number of non-synonymous mutations to generate immunogenic tumor neoantigens, which can be recognized and presented by antigen presentation cells, thereby eliciting T cell responses¹³. However, MSI-H GCs represent only 10–15% of all GCs, and this proportion further decreases to 5% in advanced cases, limiting the clinical benefits of ICIs in GCs substantially¹⁴. Given the large number of MSS GCs, there is an urgent need for reliable biomarkers to pre-select ICI-responsive MSS patients.

Numerous efforts have been made to identify therapeutic biomarkers in MSS GCs. Higher tumor mutational burden (TMB) correlates with a better clinical response to ICIs in KEYNOTE-062, but its predictive value is diminished when MSI-H patients are excluded¹⁵. In KEYNOTE-059, ORR increased from 9% in unstratified MSS GCs to 17.4% in patients with a combined positive score (CPS) of PD-L1 ≥ 10¹¹. However, the calculation of CPS is subject to pathologists’ subjective bias, severely limiting CPS’s clinical applications. A retrospective analysis of 61 advanced GC patients who received PD-1 antibodies declared a 100% ORR in Epstein–Barr virus (EBV)⁺ MSS GC patients¹⁶. This result garnered global attention regarding the role of EBV status in ICI responses. In follow-up studies, EBV⁺ MSS GCs demonstrated an ORR ranging from 25% to 33%^{17–19}. Although standard operating procedures can be optimized to improve the consistency of test methods, their accuracies in predicting ICI responses are far from satisfactory.

The fundamental inadequacy in current biomarkers is that they only capture the tumor-intrinsic factors of GCs, while the intricate nature of tumor microenvironment (TME) has been largely overlooked. TME is a complex ecosystem comprised of numerous cellular and non-cellular components intertwined with delicate interactions²⁰. Recent advances in high-resolution techniques (multiplex immunohistochemistry, spatial RNA-sequencing, and single-cell RNA-

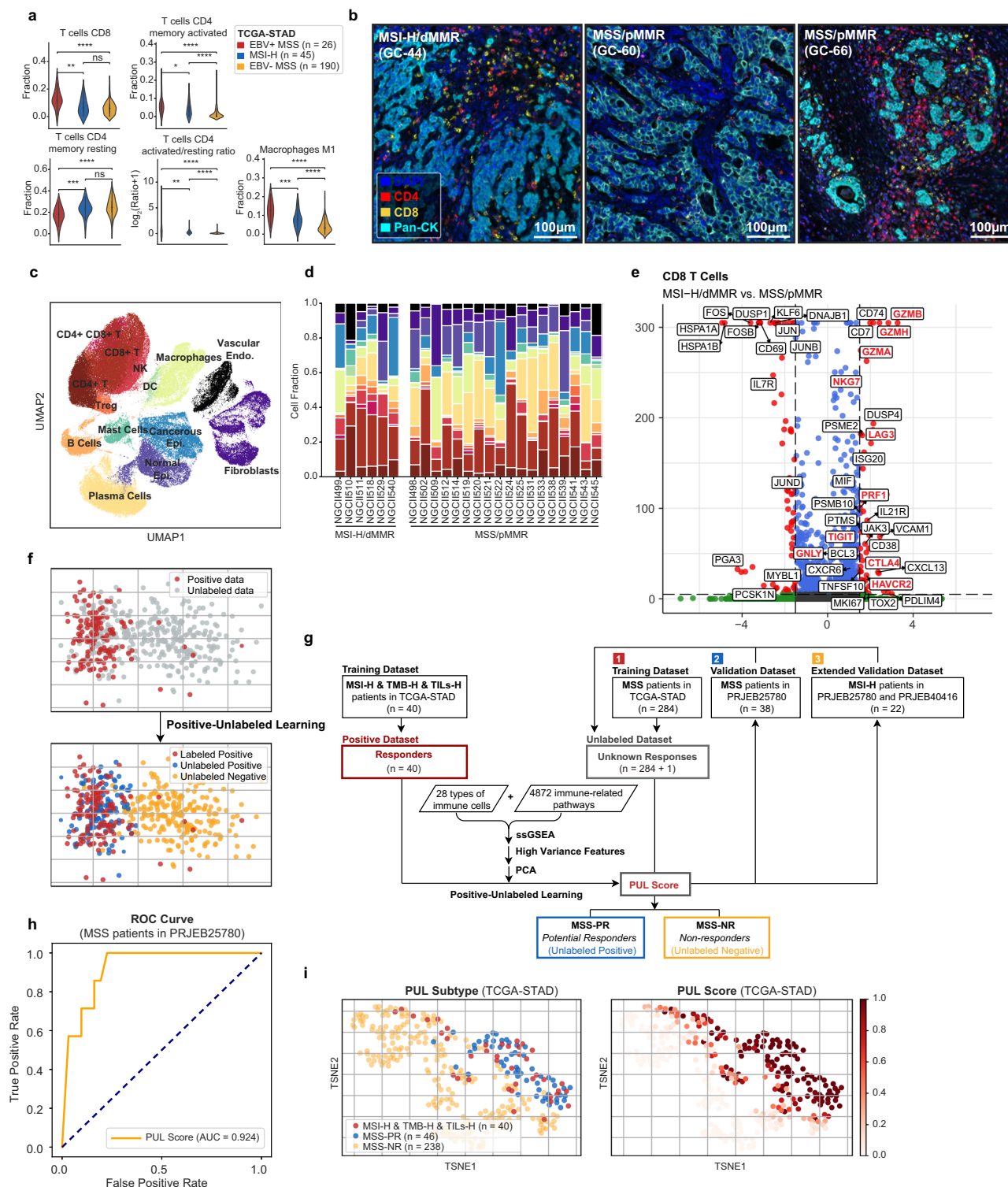
sequencing) and machine learning facilitate the study of TME complexity^{21–23}. Tumor-infiltration lymphocytes (TILs) are the predominant anti-tumor cells in the TME and the direct targets of ICI therapy. Understanding the functional heterogeneity of TILs provides insights into the determinants of varied ICI responses in cancers and, most importantly, offers potential strategies for weaponizing immune cells to target tumors.

In this study, we utilize semi-supervised machine learning to identify potential responders in MSS GCs (MSS-PRs) with a TME favorable for ICI efficacy. Comprehensive evaluation of MSS-PRs’ TME reveals that T-bet⁺ CD8⁺ T cells govern ICI responses in MSS GCs through superior anti-tumor ability and initiation of an immune-active microenvironment via a positive-feedback loop with PD-L1⁺ tumor cells. Adoptive transfer of T-bet⁺ CD8⁺ T cells reinvigorates tumor immune microenvironment and sensitizes immune-ignorant tumors to ICIs in humanized mice models. Altogether, our study underscores the crucial role of T-bet⁺ CD8⁺ T cells in driving ICI responses and offers strategies to overcome the current therapeutic bottleneck of poor ICI efficacy in MSS GCs.

Results

Patient Characteristics and Clinical Outcome

We retrospectively collected clinical information of advanced gastric cancer patients who have received PD-1 inhibitor treatment (GC-ICI cohort) (*n* = 25, Table 1) at First Hospital of China Medical University, from May 2019 to December 2021. Patients in GC-ICI cohort have completed at least two cycles of standard-of-care PD-1 inhibitor treatment and were evaluated for response according to RECIST 1.1, with a median follow-up time of 135 days. Complete response (CR) was not achieved in our cohort, 7 patients achieved partial response (PR), 15 patients achieved stable disease (SD), and 3 had progressed disease (PD).



A total of 120 patients with stage I-III gastric adenocarcinoma who received surgery at the First Hospital of China Medical University were included in the GC cohort, with a median follow-up time of 117 months. In the GC cohort, 5.83% (7/120) patients are MSI-H/dMMR, lower than that of 18.16% (63/347) in TCGA-STAD cohort, and 11.27% (31/275) in ACRG cohort²⁴. Clinical characteristics of GC patients were described in Supplementary Table 1.

Immune heterogeneity in different GC subtypes

MMR Status and EBV status were associated with different susceptibilities to ICI therapy in multiple clinical trials^{9,11,13,15,16}. In our GC-ICI

cohort, the response rates attributed to MSI-H, EBV⁺ MSS, and EBV⁻ MSS subtypes were 57.14% (4/7), 25% (1/4), and 14.29% (2/14), respectively. To understand the determinants of varied responses, immunologic analysis of different GC subtypes based on bulk RNA sequencing, single-cell RNA sequencing (scRNA-seq), and multiplex immunohistochemistry (mIHC) was conducted. In both TCGA-STAD and ACRG cohorts, CD8⁺ T cells were most abundant in EBV⁺ MSS GCs estimated by CibersortX (Fig. 1a, Supplementary Fig. 1a)¹⁶. The proportion of CD8⁺ T cells in MSI-H GCs was slightly higher than EBV⁻ MSS GCs in ACRG cohort ($P = 0.05$, Supplementary Fig. 1a), but not in TCGA-STAD cohort ($P = 0.39$, Fig. 1a). CD4⁺ T cells in both EBV⁺ MSS and

Fig. 1 | Immune landscape of different GC subtypes. **a** Violin plots of immune infiltration in EBV⁺MSS ($n = 26$), MSI-H ($n = 45$), and EBV⁺MSS ($n = 190$) patients in TCGA-STAD cohort estimated by cibersortX. Two-tailed Mann-Whitney U test was used to evaluate statistical significance between every two subtypes. **b** Multiplex IHC images of an MSI-H GC patient (GC-44), an immune-ignorant MSS GC patient (GC-60), and an immune-hot MSS GC patient (GC-66). Red denotes CD4⁺ T cells; yellow denotes CD8⁺ T cells; cyan denotes tumor cells, DAPI was used as the counterstain for cellular nuclei. **c** UMAP plot of 118,887 cells in 24 gastric tumors (GSE183904). Endo. is the abbreviation for endothelial cells; DC for dendritic cells; and epi. for epithelial cells. **d** Stacked bar plots of cell fractions in MSI-H ($n = 6$) and MSS GC tumors ($n = 18$). Each color denotes a cell type, as indicated in Fig. 1c. **e** Volcano plot of differential expression genes between CD8⁺ T cells of MSI-H GCs and those of MSS GCs. The y-axis denoted the adjusted P value, and the x-axis denoted the log₂ fold change. Genes with a |log₂ fold change| ≥ 1.5 and a P value $\leq 1 \times 10^{-5}$ were shown in red. P values were calculated with Wald test using DESeq2 and adjusted using Benjamini-Hochberg method for multiple comparisons. **f** Schematic graph of the theory of positive-unlabeled learning. Original positive

and unlabeled data points were shown as red and gray dots in the original image. Unlabeled positive (blue dots) and unlabeled negative (yellow dots) data points were identified using positive-unlabeled learning. **g** Pipeline of constructing the positive-unlabeled learning models for RNA-seq data (TCGA-STAD, PRJEB25780, and PRJEB40416). The model uses MSS patients in TCGA-STAD as training dataset, and patients in PRJEB25780 and PRJEB40416 as validation datasets. Detailed methods were described in the method section. **h** The receiver operating characteristic (ROC) curve presents false-positive rates against true-positive rates of predicting responders versus non-responders in MSS patients of PRJEB25780 cohort (validation dataset) based on PUL scores (AUC = 0.924). **i** T-SNE plot of MSI-H&TMB-H&TILs-H ($n = 40$), MSS-PR ($n = 46$), and MSS-NR ($n = 238$) patients in TCGA-STAD cohort. Geographical proximity between data points denotes their similarity in immune features. Proximity between MSI-H&TMB-H&TILs-H subtype and MSS-PR subtype was observed. On the right, heatmap of PUL scores of MSI-H&TMB-H&TILs-H ($n = 40$), MSS-PR ($n = 46$), and MSS-NR ($n = 238$) patients in TCGA-STAD cohort. * $P < 0.05$; ** $P < 0.01$; *** $P < 0.001$; **** $P < 0.0001$; ns is abbreviation for not significant.

MSI-H GCs tended to polarize toward a more activated phenotype, manifested by a greater activating/resting ratio of memory CD4⁺ T cells (Fig. 1a, Supplementary Fig. 1a). In EBV⁺ MSS and MSI-H patients, tumor-associated macrophages (TAM) exhibited an M1-polarized phenotype, which is known to exhibit anti-tumor activity by activating type 1 (Th1) immunity (Fig. 1a, Supplementary Fig. 1a)²⁵. To comparing the abundance of T cells infiltration in real-world patients, we performed mIHC staining on tumor tissue of patients in the GC cohort (Fig. 1b). In the GC cohort, there is no significant difference in the abundance of CD8⁺ T cells ($P = 0.44$) or CD4⁺ T cells ($P = 0.98$) between MSI-H and MSS patients (Supplementary Fig. 1b). However, we did observe significant immune infiltration heterogeneity in the TME of GCs, which is particularly true for the MSS populations, with a Gini coefficient of 0.527 for CD8⁺ T cells and 0.529 for CD4⁺ T Cells (Supplementary Fig. 1c, d). When most of MSS GCs exhibited an immune-ignorant status, there is a small percentage of MSS GCs harbored a TME with abundant tumor-infiltrating T cells (Supplementary Fig. 1c, d).

To further investigate the functional diversities of TILs in the TME of GCs, we conducted unbiased single-cell clustering on 6 MSI-H and 18 MSS GCs, and eventually annotated 14 cell types (Fig. 1c, Supplementary Fig. 2a, b). As expected, the proportions of CD8⁺ T cells ($P = 0.22$) or CD4⁺ T cells ($P = 0.49$) in immune cells were not significantly elevated in MSI-H GCs (Fig. 1d, Supplementary Fig. 2c). However, increased levels of cytotoxic molecules (GZMB, GZMH, GZMA, GNLY, NKG7) and immune checkpoint molecules (LAG3, CTLA-4, HAVCR2/TIM-3, TIGIT) were detected in CD8⁺ T cells of MSI-H GCs (Fig. 1e, Supplementary Fig. 2d). Stimulation of tumor antigens activates anti-tumor immunity of CD8⁺ T cells, which eventually leads to T cell exhaustion in MSI-H GCs. All the results above demonstrated that the immune heterogeneity of different GC subtypes existed not only in immune cell compositions but also in functional diversities and intriguing intracellular interactions.

Semi-supervised learning identifies potential responders in MSS GCs

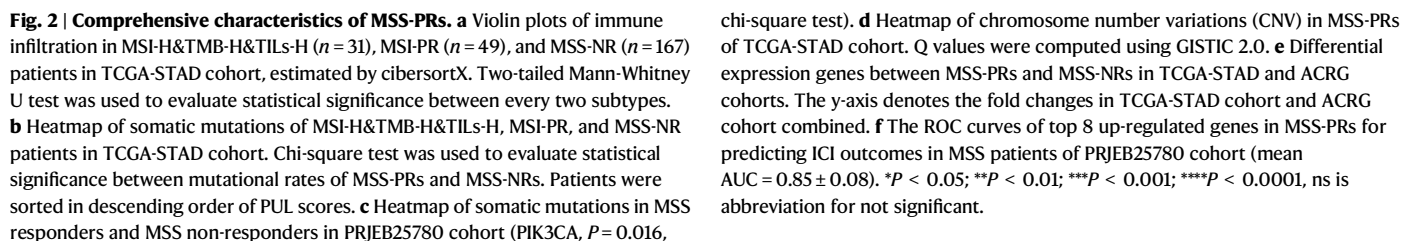
An inflamed TME characterized by rich infiltration of cytotoxic lymphocytes (CTLs) is the key to ICI susceptibility^{20,26}. Compared to EBV⁺ MSS GCs, MSI-H GCs, and EBV⁺ MSS GCs were noted by a similar inflamed TME and consequently exhibited higher response rates to ICI therapy (Fig. 1a, Table 1, Supplementary Fig. 1a). Therefore, we hypothesize that MSS GCs with a similar TME of MSI-H GCs would likely be potential ICI responders.

Positive-Unlabeled Learning (PUL) is a semi-supervised learning algorithm that learns from only positive and unlabeled samples. This machine learning algorithm applies when the available training set consists of an incomplete dataset of positive samples and an unlabeled

dataset that includes both positive and negative samples²⁷ (Fig. 1f). Therefore, to identify potential ICI responders in MSS GC (MSS-PRs), PUL was performed regarding MSI-H GC patients with a high TMB and abundant T-cell infiltration (those most likely to respond to ICIs) as positive samples, whereas MSS GC patients with undetermined responses as unlabeled samples (Fig. 1g, Supplementary Fig. 3a). We first sought to comprehensively characterize the immunologic contexts of GCs by constructing immune-related features based on the abundance of immune cells and the activities of immune-related pathways (Fig. 1g, Supplementary Fig. 3b, Supplementary Data File 1). We then trained a 1000-iteration bagging supporting vector machine (SVM) PUL model on a reduced 5-dimensional feature to identify MSS-PRs from the unlabeled MSS GCs (Fig. 1g, Supplementary Fig. 3c, Supplementary Data File 1)²⁸. A PUL score was predicted for each sample in the unlabeled dataset, which is calculated by the times of specific sample was predicted as positive divided by the total iteration of 1000. The closer the PUL score is to 1, the more likely the MSS patient would respond to ICI therapy. To independently validate the accuracy of PUL model, MSS GCs from PRJEB25780 cohort, who have been treated with PD-1 inhibitors, were included in the validation dataset¹⁶. Surprisingly, the PUL model performed exceptionally well at identifying ICI responders from MSS GCs, with an AUC of 0.924, making it currently the most accurate model for the purpose (Fig. 1h). The optimal cut-off of 0.953 was determined to maximize the sensitivity and specificity for distinguishing MSS-PRs and non-responders in MSS patients (MSS-NRs). MSS GCs in PRJEB25780 cohort with a PUL score ≥ 0.953 had an ORR of 100% to PD-1 inhibitors (Supplementary Fig. 2d, Supplementary Data File 2). The proportion of MSS-PRs in MSS GCs was 19.37% in TCGA-STAD cohort and 11.07% in ACRG cohort, comparable with reported ORRs in various clinical trials^{11,12} (Fig. 1i, Supplementary Fig. 3e, Supplementary Data File 2). Furthermore, we include MSI-H GCs from PRJEB25780 and PRJEB40416 cohorts in the extended datasets^{16,29} (Fig. 1g). The PUL model achieved an AUC of 0.821 at identifying ICI responders in MSI-H GCs, making it the most accurate model for GCs regardless of patients' microsatellite status (Supplementary Fig. 4a–c).

Comprehensive Characteristics of MSS-PRs

To comprehensively depict the characteristics of MSS-PRs, we performed a multi-dimensional differential analysis between MSS-PRs and MSS-NRs, regarding immune infiltration, single nucleotide polymorphism (SNP), copy number alterations (CNV), and transcriptomic expression. As expected, the immune profile of MSS-PRs resembled that of MSI-H & TMB-H & TILs-H patients (positive samples), characterized by a higher infiltration of CD8⁺ T cells, activated CD4⁺ memory T cell and M1-polarized macrophages (Fig. 2a, Supplementary



(Supplementary Data File 2). TMB was significantly higher in MSS-PRs than in MSS-NRs, but its utility as a therapeutic biomarker was limited by its relatively low accuracy in response prediction (AUC = 0.623, Supplementary Fig. 5d, e).

Multi-omics analysis revealed several genetic alterations were more prevalent in MSS-PRs (Supplementary Data File 3). Among them, PIK3CA mutation was most prominently associated with a better response to ICIs, with 60% of PIK3CA mutant MSS GCs being potential responders, compared to 15.44% of PIK3CA wild-type MSS GCs (Fig. 2b). In PRJEB25780 cohort, PIK3CA mutant MSS GCs had a 75% ORR to ICIs, while the ORR for PIK3CA wild-type MSS GCs was only 14.6% (Fig. 2c). Moreover, we found that PIK3CA mutant MSS GCs exhibited an inflamed TME, characterized by an increase in CD8⁺ T cell infiltration and CD4⁺ memory cell activation (Supplementary Fig. 5f). We discovered that somatic amplification of 9p24.1, containing multiple critical genes such as PD-L1 and PD-L2, occurred frequently in MSS-PRs but not in MSS-NRs (Fig. 2d). Interestingly, we found that 9p24.1 amplification and PIK3CA mutation were not only detected in EBV⁺ MSS GCs as previously reported, but also exist in other EBV⁻ MSS-PRs, indicating that these genetic alterations may be potential tumor-intrinsic mechanism to drive ICI susceptibility, independent of patients' EBV status^{30,31} (Fig. 2d).

Differential expression genes (DEGs) between MSS-PRs and MSS-NRs implied underlying determinants of ICI responses (Supplementary Data File 4). We noticed that CXCR3-ligands (CXCL9, CXCL10, and CXCL11) were among the most significantly up-regulated genes in MSS-PRs (Fig. 2e). CXCL9/10/11 are known to be up-regulated in an interferon- γ (IFN- γ) dependent manner³². Intriguingly, MSS-PRs also exhibited elevated levels of IFNG and numerous other interferon-stimulating genes (ISGs, including IDO1, CD274/PD-L1, WARS, and GBP1/4/5) (Fig. 2e). In addition, multiple cytotoxic molecules (GZMB, GNLY, GZMA, GZMH, NKG7, PRF1) and immune checkpoints (KLRC1, FASLG, LAG3, KLRD1) were also up-regulated in MSS-PRs (Fig. 2e). Top up-regulated DEGs demonstrated remarkable accuracy in predicting ICI responses of MSS patients, with an average AUC of 0.85 (Fig. 2f, Supplementary Fig. 3g).

T-bet⁺ T cells exhibit superior anti-tumor immunity

The up-regulated genes in MSS-PRs highlighted the importance of IFN- γ signaling pathway and CXCR3-CXCL9/10/11 chemotaxis pair for ICI outcomes. CXCR3 and IFNG are the direct transcription targets of the immune cell-specific T-box transcription factor T-bet, which have been studied exclusively in the past decade^{33–35}. To our surprise, apart from classic transcription targets of T-bet, multiple cytotoxic molecules, such as GZMB, PRF1, NKG7, GZMH, and GNLY, were also upregulated in tumor-infiltrating T-bet⁺ T cells, verified by both flowcytometry and scRNA-Seq (Fig. 3a, b, Supplementary Fig. 6a–f). The vast overlap between up-regulated genes in MSS-PRs and T-bet-regulated genes implied a potentially critical role of T-bet⁺ T cells in ICI outcomes and anti-tumor immunity.

Multiplex IHC confirmed the co-expression of CXCR3 with T-bet in tumor-infiltrating CD4⁺ and CD8⁺ T cells (Fig. 3c). We speculated that T-bet⁺ T cells could be chemoattracted to tumor cores via CXCL9/10/11-CXCR3 chemotaxis and exhibit anti-tumor activity by secreting IFN- γ , granzyme B and multiple other cytotoxic molecules (Fig. 3d). To test the hypothesis, we quantified the proportion of T-bet⁺ and T-bet⁻ T cells in 19 gastric tumors (18 MSS GCs and 1 MSI-H GC) from adjacent normal tissue (N), normal-tumor margins (M), tumor edges (E), to tumor cores (C) using mIHC. From N to C, the proportions of CD8⁺ T cells in the stroma compartments gradually decreased. The proportions of CD4⁺ T cells peaked at tumor edges and dropped precipitously before entering tumor cores (Fig. 3e). Intriguingly, the proportions of both T-bet⁺ CD8⁺ and T-bet⁺ CD4⁺ T cells constantly increased from N to C, demonstrating that T-bet⁺ T cells had a greater ability to infiltrate into tumor cores, possibly as a result of chemotaxis by CXCL9/10/11-CXCR3 chemotaxis pair (Fig. 3e).

Consistent with previous studies, IFN- γ and granzyme B expressions were dramatically elevated in CD8⁺ T cells following induction of T-bet expression by IL-12³⁵ (Supplementary Fig. 7a–d). To evaluated

T-bet⁺ T cells' anti-tumor ability in vivo, we transferred T-bet^{high} or T-bet^{low} T cells into peripheral circulation of tumor-bearing humanized mice (Fig. 3f). As expected, mice transferred with T-bet^{high} T cells experienced a significant reduction in tumor sizes compared to the control mice transferred with T-bet^{low} T cells (Fig. 3g, Supplementary Fig. 8a). The TME of T-bet^{high} T cells-transferred mice were richly infiltrated with T-bet⁺ CD8⁺ and T-bet⁺ CD4⁺ T cells, whereas T-bet^{low} T cells-transferred mice remained immune ignorant, as evidenced by both mIHC and intratumoural flow cytometry (Fig. 3h, i, Supplementary Fig. 8b). Tumor-infiltrating T-bet⁺ CD4⁺ or CD8⁺ T cells also exhibit greater cytotoxicity than T-bet⁻ CD4⁺ or CD8⁺ T cells with higher levels of granzyme B and IFN- γ . (Fig. 3j, Supplementary Fig. 8c, d).

To verify the anti-tumor activity of tumor-infiltrating T-bet⁺ T cells in real-world GC patients, we calculated the percentages of T-bet⁺ CD8⁺ T cells and T-bet⁺ CD4⁺ T cells in patients in the GC cohort using mIHC. We found that a higher abundance of T-bet⁺ CD8⁺ T cells in the TME was associated with significantly longer median OS (77.0 months vs. 24.0 months), indicating a stronger anti-tumor activity of T-bet⁺ CD8⁺ T cells (Fig. 3k). Our findings strongly suggested that T-bet⁺ T cells, especially T-bet⁺ CD8⁺ T cells, are distinct subpopulations of T cells with greater capacity to infiltrate into tumor cores and elicit superior anti-tumor activity through secreting IFN- γ and granzyme B.

T-bet⁺ CD8⁺ T cells are highly infiltrated in the tumor compartments of ICI-sensitive cancers

Surprisingly, we found that although the ratio of T-bet^{high} CD8⁺ T cells/T-bet^{high} CD4⁺ T cells was 0.36 times before transfer in the tumor-bearing humanized mice model, the ratio of tumor-infiltrating T-bet⁺ CD8⁺ T cells/T-bet⁺ CD4⁺ T cells rose to 1.67 times in the TME (Fig. 4a). Similarly, single-cell analysis of tumor-infiltrating immune cells in GCs revealed that the majority of tumor-infiltrating T-bet⁺ cells were CD8⁺ T cells, indicating a more significant role of T-bet⁺ CD8⁺ T cells in the TME of GCs (Fig. 4b, c). To further gain insights into determinants of ICI responses on a spatial level, we quantified the proportions of T-bet⁺ CD8⁺ T cells in different compartments of GCs (Fig. 4d, e). The percentages of T-bet⁺ CD8⁺ T cells continued to increase from 0.21% in the stroma compartments to 0.25% in the tumor compartments, whereas the percentage of T-bet⁺ CD4⁺ T cells decreased to approximately 50% that of T-bet⁺ CD8⁺ T cells in the tumor compartments, suggesting closer proximity of T-bet⁺ CD8⁺ T cells with tumor cells (Fig. 4f).

ICI responders and MSS-PRs were noted by a similar spatial distribution of T-bet⁺ CD8⁺ T cells in their tumor compartments, whereas non-responders exhibit little infiltration despite being MSI-H (Fig. 4g, Supplementary Fig. 9a). In the GC cohort, MSI-H GCs showed a tendency of increased T-bet⁺ CD8⁺ T cells infiltration, and 14.16% (16/113) MSS GCs have more T-bet⁺ CD8⁺ T cells infiltration than the majority of MSI-H GCs (Supplementary Fig. 9b, Supplementary Data File 5). We did not observe a difference in T-bet⁺ CD8⁺ T cells infiltration between EBV⁺ MSS GCs and EBV⁻ MSS GCs (Supplementary Fig. 9b, Supplementary Data File 5). To test whether tumor-infiltrating T-bet⁺ CD8⁺ T cells could predict ICI responses for a broader range of GC patients, we deconvoluted the proportions of tumor-infiltrating T-bet⁺ CD8⁺ T cells in patients treated by ICIs, using an immune cell matrix generated from scRNA-seq data (Supplementary Data File 6). We found that a higher abundance of T-bet⁺ CD8⁺ T cells was associated with better ICI responses in both MSS and MSI GCs, with an AUC of 0.800 and 0.775, respectively (Fig. 5h, i).

T-bet⁺ CD8⁺ T cells sensitize immune-ignorant GCs to ICI therapy

Tumor-infiltrating T-bet⁺ CD8⁺ T cells exhibited superior anti-tumor activity and were predictive of ICI responses in MSS GCs, as evidenced by their greater ability to infiltrate into tumor cores

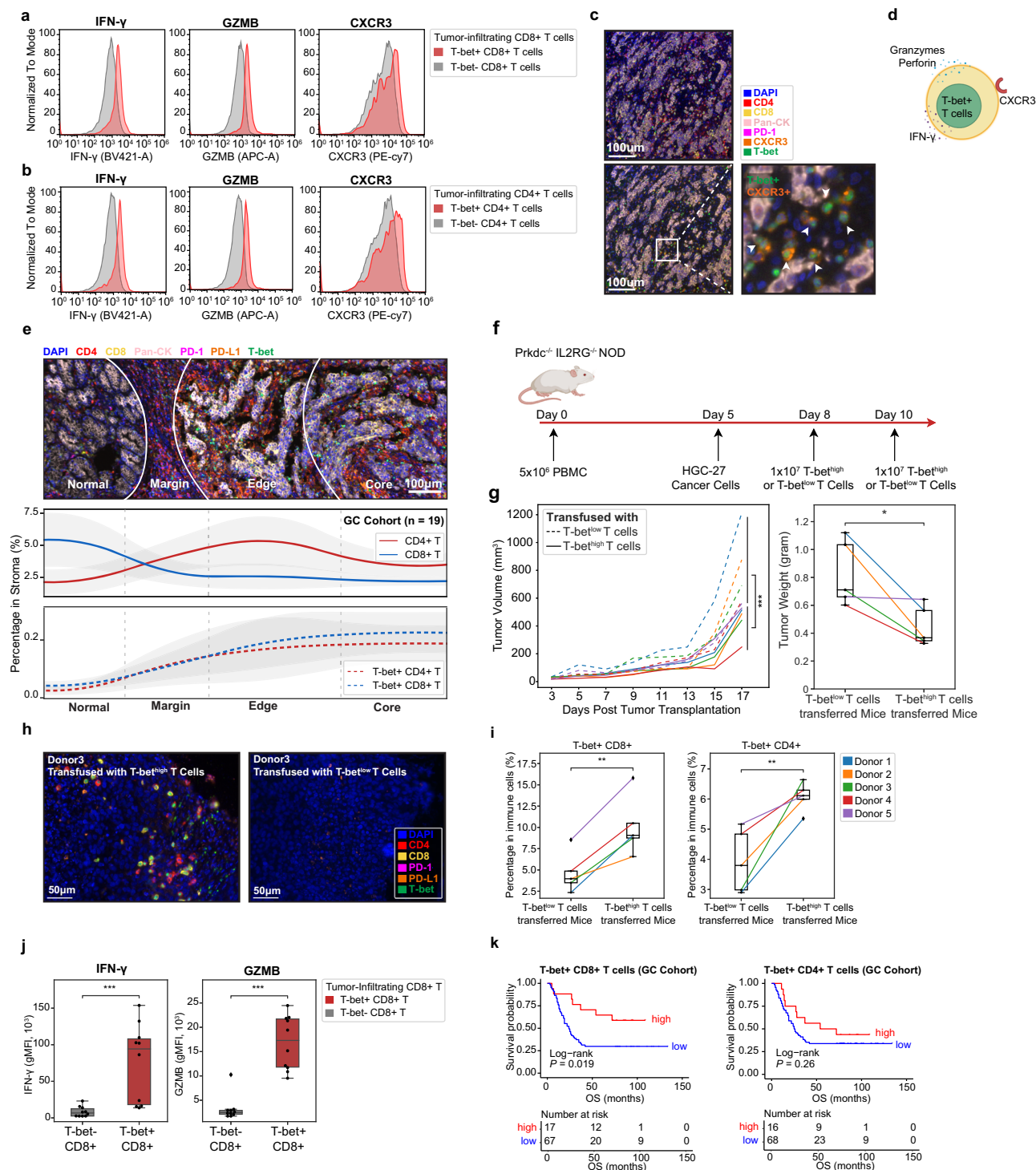


(Fig. 4a, d–f) and a stronger association with longer OS in GC patients (Fig. 3k). We sought to evaluate whether adoptive transfer of T-bet^{high} CD8⁺ T cells could improve ICI outcomes in immune-ignorant MSS GCs. To mimic the TME of immune-ignorant patients, human MSS GC cells were subcutaneously injected into immunodeficient NYG mice to generate immune-ignorant tumor grafts, which were then evenly transplanted subcutaneously into humanized mice (Fig. 5a). T-bet^{high} CD8⁺ or T-bet^{low} CD8⁺ T cells were injected through the tail vein of tumor-bearing humanized mice on two consecutive occasions. PD-1 inhibitor or IgG4 isotype was administered every two days (Fig. 5a). At the endpoints, we observed that ICI efficacy was significantly enhanced in T-bet^{high} CD8⁺ T cells-transferred mice (Fig. 5b,

Supplementary Fig. 10a). In T-bet^{low} CD8⁺ T cells-transferred mice, anti-PD-1 antibody decreased tumor sizes by 45.2% compared to isotype administration. This number went up to 68.3% in T-bet^{high} CD8⁺ T cells-transferred mice (Fig. 5b). Combined therapy of T-bet^{high} CD8⁺ T cell transfer and anti-PD-1 antibody significantly increased immune infiltration in mice's tumor cores, confirmed by both mIHC and intratumoural flow cytometry (Fig. 5c, d, Supplementary Fig. 10b). We conclude that T-bet^{high} CD8⁺ T cells improve anti-tumor immunity and confer ICI susceptibility in immune-ignorant GCs. This combined regimen could revolutionize the current treatment options for immune-ignorant GCs, which account for the majority of advanced GC cases.

Fig. 3 | T-bet⁺ T cells exhibit superior anti-tumor immunity. **a** Flow cytometer analysis of expression of IFN- γ , GZMB, and CXCR3 in T-bet⁺ CD8⁺ ($n = 1675$) and T-bet⁺ CD8⁺ T cells ($n = 12,852$). **b** Flow cytometer analysis of expression of IFN- γ , GZMB, and CXCR3 in T-bet⁺ CD4⁺ ($n = 1778$) and T-bet⁺ CD4⁺ T cells ($n = 19,704$). **c** T-bet⁺ CD4⁺ T cells, T-bet⁺ CD8⁺ T cells, and T-bet⁺ CXCR3⁺ cells exist in the TME of GC tumors. MHC images were taken from GC patients in the GC cohort. **d** Downstream genes of the transcription factor T-bet. In T cells, GZMB, PRF1, IFNG and CXCR3 are the direct targets of T-bet (Created in BioRender. Tang, Shiyang. (2025): <https://biorender.com/y38v503>). **e** Line plots of average percentages of CD4⁺ T cells, CD8⁺ T cells, T-bet⁺ CD4⁺ T cells, and T-bet⁺ CD8⁺ T cells in the stroma compartments of normal tissue (N), normal-tumor margins (M), tumor edges (E), and tumor cores (C) ($n = 19$, 1 MSI-H GC, 4 EBV⁺ MSS GCs, 14 EBV⁻ MSS GCs). Gray margins indicate standard errors. Original line plots were interpolated using interp1d function in SciPy (v 1.8.1). **f** Schematic graph of constructing tumor-bearing humanized mice model (Created in BioRender. Tang, Shiyang. (2025): <https://biorender.com/r39f251>). **g** Line plot of tumor volumes over time ($P = 2.197 \times 10^{-4}$, two-tailed two-way ANOVA test, using time and group as two independent variables). Tumor volumes were calculated as $1/2 \times (\text{Length} \times \text{Width}^2)$. On the right, box plot of tumor weights at endpoints of mice transfused with T-bet^{high} or T-bet^{low} T cells ($P = 0.0292$, two-tailed paired-wise t-test. $n = 5$ biologically replicates from 5

different healthy PBMC donors). **h** mIHC of tumor-infiltrating T-bet⁺ CD4⁺ T cells and T-bet⁺ CD8⁺ T cells in humanized mice transfused with T-bet^{high} or T-bet^{low} T cells. **i** Box plots of percentages of T-bet⁺ CD8⁺ T cells ($P = 2.434 \times 10^{-3}$, two-tailed paired-wise t-test) and T-bet⁺ CD4⁺ T cells ($P = 9.848 \times 10^{-3}$, two-tailed paired-wise t-test) in tumor-infiltrating immune cells, comparing mice transfused with T-bet^{high} T cells with mice transfused with T-bet^{low} T cells ($n = 5$, biologically replicates from 5 different healthy PBMC donors). Original data was generated by flow cytometer analysis. **j** Box plots of geometric mean fluorophore intensities (gMFIs) of IFN- γ ($P = 7.685 \times 10^{-4}$, two-tailed Mann-Whitney U test) and GZMB ($P = 2.461 \times 10^{-4}$, two-tailed Mann-Whitney U test) in T-bet⁺ CD8⁺ T cells and T-bet⁺ CD8⁺ T cells from 10 CDX GC tumors. **k** Kaplan-Meier curves of overall survival in patients in the GC cohort in relationship to T-bet⁺ CD8⁺ T cell abundance (on the left) and T-bet⁺ CD4⁺ T cell abundance (on the right). The percentages were calculated as the number of T-bet⁺ CD8⁺ or CD4⁺ T cells divided by the number of all cells in respective patient. A percentage of 0.2% was set as the cutoff to distinguish high or low infiltration of T-bet⁺ CD8⁺ and T-bet⁺ CD4⁺ T cells. * $P < 0.05$, ** $P < 0.01$, *** $P < 0.001$, **** $P < 0.0001$, ns is abbreviation for not significant. **g, i, j** In the box plots, the bounds of the box span from 25% to 75% percentile, the line represents the median, and the whiskers show the 1.5 Interquartile range (IQR) of the data points.

Positive-feedback loop between T-bet⁺ T cells and PD-L1⁺ tumor cells drives ICI sensitivity

We then sought out to identify the intracellular communications between T-bet⁺ CD8⁺ T cells and other cell types in GCs, using scRNA sequencing. Not surprisingly, T-bet⁺ CD8⁺ T cells are the most important overall incoming signaling receivers in both MSI-H and MSS GCs (Supplementary Fig. 11a). However, only in MSI-H GCs, T-bet⁺ CD8⁺ T cells interact with a wide range of other cell types (such as macrophages, dendritic cells, cancerous epithelial cells, CD8⁺ T cells, and Treg), whereas in MSS GCs, the communications are limited within fibroblasts and vascular endothelial cells (Supplementary Fig. 11b). T-bet⁺ CD8⁺ T cells in MSI-H GCs also show higher expression of cytotoxic molecules and HLA molecules than those in MSS GCs, implicating a stronger cytotoxic phenotype of T-bet⁺ CD8⁺ T cells could also be driven by tumor innate characteristics (Supplementary Fig. 11c).

We further examined the TME of ICI-sensitive GCs, and found that T-bet⁺PD-L1⁺ niches were frequently observed in patients and humanized mice with abundant infiltration of T-bet⁺ CD8⁺ T cells (Figs. 5e, 6a, Supplementary Fig. 12a). We hypothesized that higher expression of PD-L1 (and other ISGs) was induced by IFN- γ -secreting T-bet⁺ T cells in the niches. We calculated the percentage of PD-L1⁺ cells in the neighboring cells (within a radius of 50 μ m) of T-bet⁺ or T-bet⁻ T cells (Fig. 6b). There was a significantly increased proportion of PD-L1⁺ cells in T-bet⁺ T cells' neighboring cells: 1.19% of T-bet⁺ CD8⁺ cells' neighboring cells were positive for PD-L1, and 4.82% for T-bet⁺ CD8⁺ cells' neighboring cells; 0.86% of T-bet⁻ CD4⁺ T cells' neighboring cells were positive for PD-L1, and 2.93% for T-bet⁻ CD4⁺ T cells' neighboring cells (Fig. 6c). To further dissect the transcriptional characteristics of T-bet⁺PD-L1⁺ niches, spatial RNA-seq analysis was performed on an ICI responder and an MSS-PR patient (Fig. 6d, Supplementary Fig. 12b). From the edge to the center of T-bet⁺PD-L1⁺ niches, there was a continuous increased level of numerous genes (e.g., IDO1, CXCL9/10/11, IFNG, GZMB, GNLY, and CCL18), creating a chemotaxis gradient for T-bet⁺ T cells to migrate (Fig. 6e). In T cell migration assay, the chemotaxis of T-bet⁺ CD8⁺ T cells to HGC-27 gastric cancer cells was significantly decreased after adding IFN- γ neutralizing antibody or CXCR3 antagonist to the medium (Supplementary Fig. 13a, b). This result suggests that chemotaxis of T-bet⁺ CD8⁺ T cells to tumor cells were orchestrated by IFN- γ .

Therefore, we propose a positive-feedback loop between T-bet⁺ T cells and PD-L1⁺ tumor cells (ISGs⁺), mediated by IFN- γ signaling pathway and CXCL9/10/11-CXCR3 chemotaxis pair, which eventually drives ICI sensitivity in GC patients (Fig. 6f). T-bet⁺ CD8⁺ T cells are chemoattracted to the tumor cores through CXCL9/10/11-CXCR3

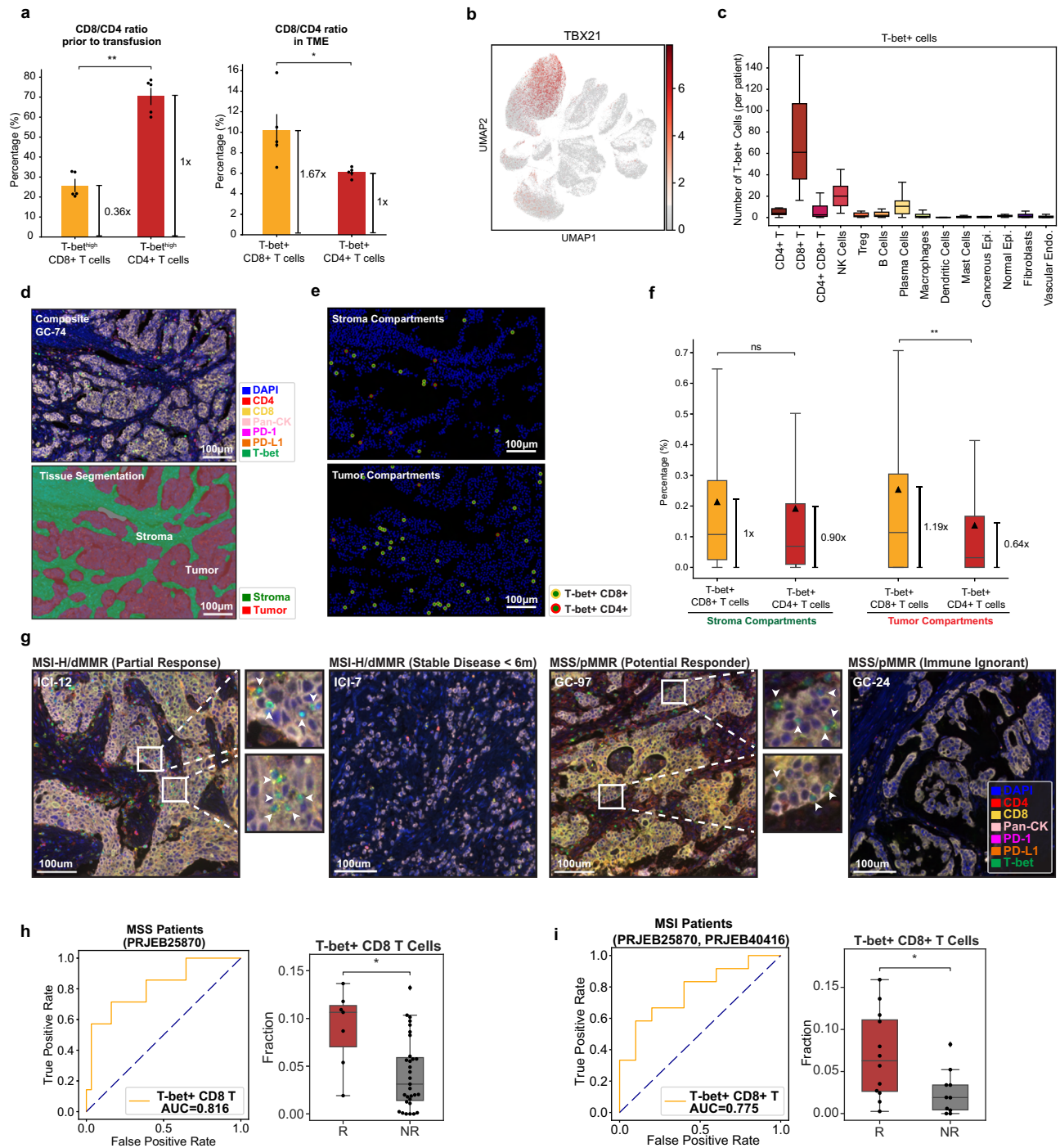
chemotaxis pair and consequently form a niche of high IFN- γ environment. IFN- γ up-regulate CXCL9/10/11, PD-L1, and other ISGs in neighboring tumor cells. As a result, more T-bet⁺ T cells are chemoattracted into the niches to exhibit cytotoxicity, and IFN- γ further up-regulate T-bet expression in other T cells, and at the meantime, drives a stronger cytotoxic phenotype of T-bet⁺ T cells. Induction of PD-L1 expression on neighboring cells and antigen-driving exhaustion of CD8⁺ T cells provide optimal pre-conditions for ICIs to exert their therapeutic effects. This positive-feedback loop, visualized in mIHC as a distinct T-bet⁺PD-L1⁺ niche, is the landmark of pre-existing suppressed anti-tumor immunity and conceptualizes the complex interplay between anti-tumor immunity and ICI susceptibility.

Discussion

In this study, we challenged the long-established problem of the lack of ICI responses in MSS GCs, by stratifying patients into MSS-PRs and MSS-NRs. The positive-unlabeled learning model demonstrated an AUC of 0.924 for predicting ICI responses in MSS GCs, making it the most accurate model currently available. We identified 19.37% of MSS GCs in TCGA-STAD cohort and 11.07% in ACRG cohort as potential responders, aligning with published data that approximately 10–15% of MSS GCs respond to ICIs^{9,11}. Here, we demonstrate how cutting-edge machine learning can be effectively applied to medical research to solve an otherwise challenging clinical problem.

Our GC-ICI cohort observed a 25% ORR in advanced EBV⁺ MSS GCs treated with standard-of-care ICI regimens; divergent ORRs ranging from 25%–100% were reported in other clinical trials^{16–19}. Using the PUL model, we found that 62.96% of EBV⁺ MSS GCs in TCGA-STAD cohort and 16.67% in ACRG cohort were potential ICI responders. The divergent proportions of responders in EBV⁺ MSS GCs between cohorts may be due to small sample sizes, the use of inconsistent testing methods, different demographic characteristics of patients, or different prior lines of treatment patients have received. While standardized testing protocols can be optimized to validate EBV status's significance on ICI responses, we found that PIK3CA mutation and 9q24 amplification that were once considered common features of EBV⁺ MSS GC were associated with a better response to ICIs in MSS GCs regardless of patients' EBV status. In this regard, we propose that these specific genetic alterations are more appropriate than EBV status as therapeutic biomarkers and, hopefully, potential drug targets.

Several studies have addressed the importance of CXCR3 and its ligands CXCL9/10/11 in anti-tumor immunity. Using bone marrow chimeric mouse models, Chow et al. demonstrated the necessity of intratumoral CXCR3⁺ CD8⁺ T cells for anti-tumor activity and ICI



efficacy³⁶. Through spatial scRNA-seq of colorectal cancers (CRCs), Pelka et al. found that the CXCR3-ligand⁺ multicellular hub is unique in dMMR CRCs, not in pMMR CRCs³⁷. Previous studies reported that T-bet is the direct transcription factor for CXCR3 and granzyme B in CD8⁺ T cells^{38–40}. We observed that T-bet⁺ CD8⁺ T cells were also positive for CXCR3 and were abundant in the tumor compartments of ICI responders, MSI-H GCs, and MSS-PRs. Consistent with published data, we proved that T-bet⁺ CD8⁺ T cells are capable of producing large quantities of cytotoxic granzymes and IFN- γ both in vitro and in humanized mice, resulting in their superior anti-tumor activity. Recent studies reported that MSI-H patients deficient in cGAS-STING or IFN- γ signaling pathway fail to respond to ICIs^{41–43}. T-bet is the master transcription factor of Th1 phenotype and is responsible for the rapid production of IFN- γ ^{39,44}. We demonstrate an

underlying relationship between CXCR3 chemotaxis pair and interferon-signaling pathway, coupled by T-bet⁺ CD8⁺ T cells, that eventually shapes an ICI-sensitive TME. After chemoattracted to the tumor cores through CXCL9/10/11 chemotaxis, T-bet⁺ CD8⁺ T cells consequently formed a niche of high IFN- γ and ISGs (e.g., CXCL9/10/11, PD-L1) environment. The positive-feedback loop between CXCR3-ligands⁺ tumor cells and T-bet⁺ T cells, manifested as T-bet⁺-PD-L1⁺ niches in mIHC, can be observed in patients with increased susceptibility to ICIs.

CPS of PD-L1 is currently the most used biomarker of ICI responses across cancer types⁴⁵. However, its accuracy is still relatively low and there is insufficient evidence to support the use of CPS as opposed to other PD-L1 scoring methods. Several studies also suggest that inducible PD-L1 has a better predictive value than constitutive

Fig. 4 | Tumor-infiltrating T-bet⁺ CD8⁺ T cells are predictive of ICIs responses in GC patients. **a** On the left, bar plots of CD8/CD4 ratio prior to transfusion ($n = 5$). The proportion of CD8⁺ T cells is 0.36 times that of CD4⁺ T cells ($P = 0.008$, two-tailed Mann-Whitney U test). On the right, bar plots of CD8/CD4 ratio in the TME of GCs ($n = 5$). The proportion of T-bet⁺ CD8⁺ T cells rose to 1.67 times that of T-bet⁺ CD4⁺ T cells ($P = 0.016$, two-tailed Mann-Whitney U test). Data were acquired by flow cytometry. Data are presented as mean \pm standard error of the mean (s.e.m.). **b** UMAP plot of TBX21 (encoding T-bet) expression across cell types in GC tumors. **c** Box plots of numbers of T-bet⁺ cells in different cell types in GC tumors. In the TME of GC patients ($n = 24$), most T-bet⁺ cells are CD8⁺ T cells. **d** Process of tissue segmentation using inFrom software (v 2.3.0). Red areas represent the tumor compartments, and green areas represent the stroma compartments. Tissue segmentation was performed based on the expression pattern of pan-CK. **e** Scoring maps in the tumor and stroma compartments. Cells with green nucleus and yellow membrane were T-bet⁺ CD8⁺ T cells; cells with green nucleus and red membrane were T-bet⁺ CD4⁺ T cells. **f** Box plots of proportion of T-bet⁺ CD8⁺ T cells and T-bet⁺ CD4⁺ T cells in the stroma compartments and tumor compartments in the GC cohort ($n = 120$). The percentage was calculated by dividing the number of non-tumor cells in respective compartments. The triangles mark the mean value of each group. In the stroma compartments, T-bet⁺ CD8⁺ T cells were more abundant than T-bet⁺ CD4⁺ T cells (0.21% vs. 0.19%, $P = 0.068$, two-tailed Mann-Whitney U test). In

the tumor compartments, T-bet⁺ CD8⁺ T cells were more abundant than T-bet⁺ CD4⁺ T cells (0.25% vs. 0.14%, $P = 0.0018$, two-tailed Mann-Whitney U test). **g** MIHC of TME of an ICI responder (ICI-12), an ICI non-responder (ICI-7), an MSS-PR patient (GC-97), and an MSS-NR patient (GC-24). T-bet⁺ CD8⁺ T cells were richly infiltrated into the tumor compartments of the ICI responder and the MSS-PR patient, as indicated by the white arrows. **h** The ROC curve for predicting of ICI responses in MSS patients based on cell fractions of tumor-infiltrating T-bet⁺ CD8⁺ T cells, estimated by CIBERSORTX (AUC = 0.816). On the right, box plot of fractions of tumor-infiltrating T-bet⁺ CD8⁺ T cells in MSS responders ($n = 7$) and MSS non-responders ($n = 31$) in PRJEB25870 cohort ($P = 0.010$, two-tailed Mann-Whitney U test). The mean value of T-bet⁺ CD8⁺ T fraction in MSS responders is 0.090. **i** The ROC curve for predicting ICI responses in MSI-H patients based on cell fractions of tumor-infiltrating T-bet⁺ CD8⁺ T cells, estimated by CIBERSORTX (AUC = 0.775). On the right, box plot of fractions of tumor-infiltrating T-bet⁺ CD8⁺ T cells in MSI responders ($n = 12$) and MSI non-responders ($n = 10$) in PRJEB25870 and PRJEB40416 cohorts. ($P = 0.032$, two-tailed Mann-Whitney U test). The mean value of T-bet⁺ CD8⁺ T fraction in MSI-H responders is 0.069. R, responders; NR, non-responders. * $P < 0.05$, ** $P < 0.01$, *** $P < 0.001$, **** $P < 0.0001$, ns is abbreviation for not significant. **c, f, h, i** In the box plots, the bounds of the box span from 25% to 75% percentile, the line represents the median, and the whiskers show the 1.5 Inter-quartile range (IQR) of the data points.

PD-L1 on tumor cells, emphasizing the importance of IFN- γ signaling pathway⁴⁶. Our mechanism-based proposal to use T-bet⁺ PD-L1⁺ niches as indicators for ICI susceptibility is more scientifically intuitive and likely more accurate than CPS of PD-L1, as it implies the adequacy of tumor-intrinsic IFN- γ signaling pathway, the presence of drug-targeted molecule PD-L1, and the abundance of tumor-infiltrating cytotoxic T cells.

Although stratifying MSS-PRs for ICI therapy can substantially broaden the benefiting spectrum of GC patients, the majority of advanced GCs remain immune-ignorant. Here, we propose to use adoptive T cell transfer (ACT) to tackle the problem. Several reasons limit the application of ACT in solid tumors: transferred T cells are difficult to be trafficked and infiltrate into tumor cores; even though they manage to infiltrate, they quickly become dysfunctional due to the hostile TME⁴⁷. We hypothesized that T-bet⁺ CD8⁺ T cells could circumvent these obstacles due to enhanced tumor-infiltrating capability and the formation of a local immune-active microenvironment. Using humanized mice model, we demonstrated that transfer of T-bet⁺ CD8⁺ T cells into tumor-bearing mice could augment anti-tumor immunity and sensitize immune-ignorant tumors to ICI treatment. Here, we provided pre-clinical evidence that combined regime of adoptive transfer of T-bet⁺ CD8⁺ T cells and PD-1 inhibitors can be leveraged to improve the clinical outcomes of immune-ignorant MSS GCs.

Given the lack of immunotherapy responses in MSS GCs, either due to the lack of reliable biomarkers to pre-select ICI candidates or due to the immune-ignorant nature of most GC cases, we approached the problem in two ways. First, we comprehensively depicted the genetic and immunologic characteristics of potential MSS GCs responders. Specific genetic alterations such as PIK3CA mutation and 9p24 amplification, as well as spatial TME features such as the abundance of T-bet⁺ CD8⁺ T cells and the presence of T-bet⁺ PD-L1⁺ niches, can be used to stratify MSS GCs for ICI treatment. Second, we demonstrated that adoptive transfer of T-bet⁺ CD8⁺ T cells could augment anti-tumor activity and confer susceptibility to ICIs in immune-ignorant MSS GCs. Altogether, our study provides insights into the underlying determinants of ICI responses in MSS GCs and offers remedies to optimize immunotherapy for immune-ignorant cancers.

Methods

Study approval

Human study protocols were approved by the Research Ethics Committee of the First Hospital of China Medical University (#2017-207) and were conducted in accordance with the Declaration of Helsinki for

Human Research. Human PBMCs were isolated from the peripheral blood of healthy donors. All participants provided written informed consent for obtaining biological specimens. Our patient cohorts included both sexes. Sex was not considered in our study design regarding patients' cohorts. All animal experiment protocols were approved by the Research Ethics Committee of China Medical University (#CMUXN2021712). To avoid the influence of hormones on mice, only female mice were used in animal studies.

Patient Characteristics and Clinical Outcome

We retrospectively collected clinical information of advanced gastric cancer patients who have received PD-1 inhibitor treatment (GC-ICI cohort) ($n = 25$, Table 1) at First Hospital of China Medical University from May 2019 to December 2021. Patients in the GC-ICI cohort have completed at least two cycles of standard-of-care PD-1 inhibitor treatment and were evaluated for response according to RECIST 1.1, with a median follow-up time of 135 days. Complete response (CR) was not achieved in our cohort; 7 patients achieved partial response (PR); 15 patients achieved stable disease (SD), and 3 patients had progressed disease (PD). Responders were defined as patients with a RECIST CR or PR, while non-responders were defined as those with SD or PD. One hundred and twenty patients with stage I-III gastric adenocarcinoma who received surgery at the First Hospital of China Medical University were included in the GC cohort, with a median follow-up time of 117 months (Supplementary Table 1). EBV status of patients in the GC cohort and GC-ICI cohort was determined by IHC staining of anti-EBV LMP1 protein (Abcam, ab7502).

Evaluation of MMR Status

Patients' MMR status was evaluated by IHC staining of four MMR proteins, MLH1 (MXB Biotechnologies, MAB-0789), MSH2 (MXB Biotechnologies, MAB-0789), MSH6 (MXB Biotechnologies, MAB-0831) and PMS2 (MXB Biotechnologies, MAB-0859). A deficiency in MMR was determined when any one of MMR proteins was absent in the nuclear staining of tumor cells, with adjacent normal tissue as positive internal control.

Bulk RNA-seq data preprocessing

Original fasta files of PRJEB25780 and PRJEB40416 were downloaded from <https://www.ebi.ac.uk/ena>. RNA sequencing reads were aligned to human reference genome (GRCh38) using STAR (version 2.6.1), followed by standard quality control and gene-level quantification to reads counts and transcript per million (TPM) by RSEM (version 1.3.1), according to the suggestions of GTEx project (<https://github.com/>

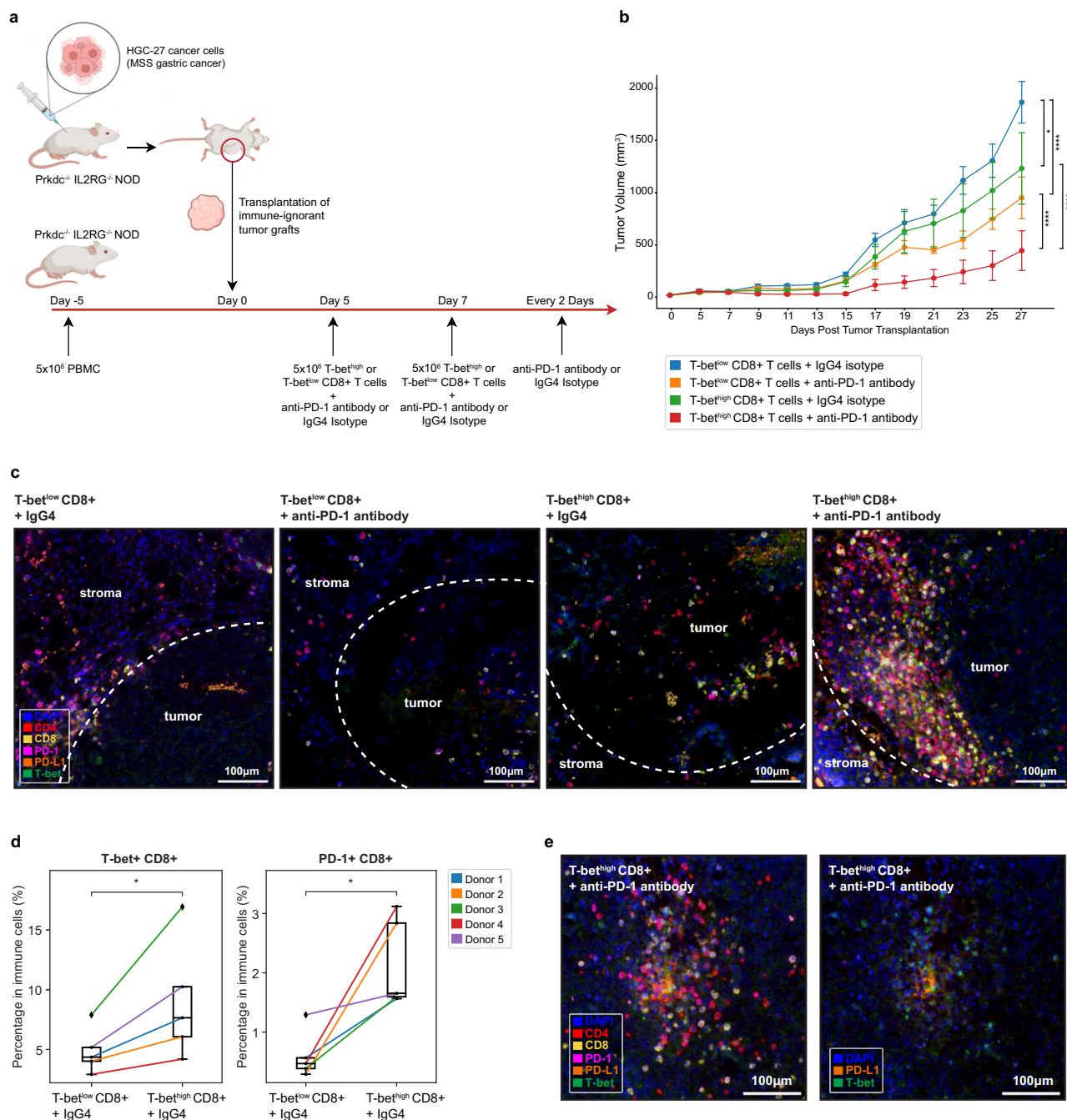


Fig. 5 | Adoptive transfer of T-bet⁺ CD8⁺ T cells confers ICI susceptibility in immune-ignorant GCs. **a** Schematic graph of constructing immune-ignorant tumor-bearing humanized mice model. Details are described in the methods section (Created in BioRender. Tang, Shiyang. (2025): <https://biorender.com/m80m221>). **b** Line plot of tumor sizes overtime (T-bet^{low} + IgG4 vs. T-bet^{high} + IgG4, $P = 0.012$; T-bet^{low} + anti-PD-1 vs. T-bet^{high} + anti-PD-1, $P = 1.191e-07$; T-bet^{low} + IgG4 vs. T-bet^{low} + anti-PD-1, $P = 3.099e-08$; T-bet^{high} + IgG4 vs. T-bet^{high} + anti-PD-1, $P = 2.201e-06$. All statistical significance was tested by two-tailed two-way ANOVA). Data are presented as mean \pm standard error of the mean (s.e.m.). **c** IHC of TME of different groups of humanized mice models. From left to right, T-bet^{low} + IgG4,

T-bet^{low} + anti-PD-1, T-bet^{high} + IgG4, and T-bet^{high} + anti-PD-1. **d** Box plots of percentages of T-bet⁺ CD8⁺ T cells ($P = 0.040$, two-tailed paired-wise t-test) or PD-1⁺ CD8⁺ T cells ($P = 0.026$, two-tailed paired-wise t-test) in tumor-infiltrating immune cells. Data was generated by flow cytometer analysis. The bounds of the box span from 25% to 75% percentile, the line represents the median, and the whiskers show the 1.5 Interquartile range (IQR) of the data points. **e** IHC images from mice treated with T-bet^{high} CD8⁺ T cells + anti-PD-1. On the left, composite image of dapi, CD4, CD8, PD-1, PD-L1, and T-bet were shown. On the right, only dapi, PD-L1, and T-bet were shown. T-bet⁺PD-L1⁺ niche can be observed. * $P < 0.05$, ** $P < 0.01$, *** $P < 0.001$, **** $P < 0.0001$, ns is abbreviation for not significant.

broadinstitute/gtex-pipeline/blob/master/TOPTMed_RNAseq_pipeline.md)^{48,49}. Raw counts of TCGA-STAD cohort were downloaded from GDC data portal (<https://portal.gdc.cancer.gov/>), and clinical data was retrieved from the original publication⁵⁰. Read counts of PRJEB25780, PRJEB40416, and TCGA-STAD datasets were normalized using ComBat-seq to remove batch effects from different experiments⁵¹.

Microarray data preprocessing

Raw expression matrix of ACRG cohort was downloaded from <https://www.ncbi.nlm.nih.gov/geo/> (accession number: GSE62254)²⁴. Probes were annotated using Affymetrix Human Genome U133plus 2.0 Array. RMA normalization was applied to remove background noises. For genes matched to multiple probes, the probe with the

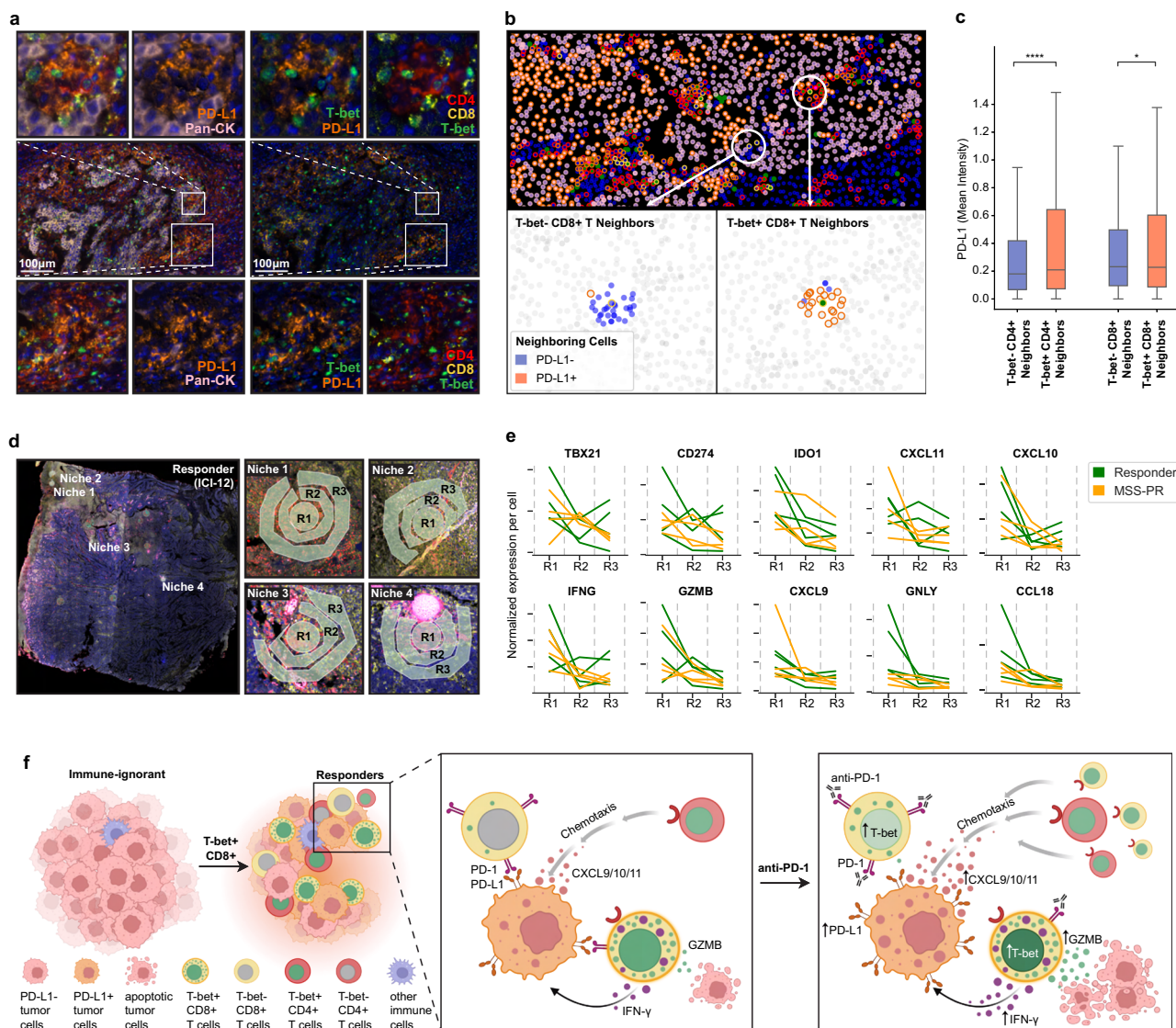


Fig. 6 | Positive feedback loop between T-bet⁺ T cells and PD-L1⁺ tumor cells drives ICI susceptibility. **a** T-bet⁺ PD-L1⁺ niches are present in patients with rich infiltration of T-bet⁺ CD8⁺ T cells (GC-44). **b** Schematic graph of neighboring cells of T-bet⁺ CD8⁺ T cells and T-bet⁺ CD8⁺ T cells. Neighboring cells were defined as cells with a distance closer than 50 μm to the original cell. Orange denotes PD-L1⁺ cells, and blue denotes PD-L1⁻ cells. **c** Box plots of mean PD-L1 intensity of the neighboring cells of T-bet⁺ CD8⁺ T cells, T-bet⁺ CD8⁺ T cells, T-bet⁺ CD4⁺ T cells, and T-bet⁺ CD4⁺ T cells in the GC cohort (T-bet⁺ CD8⁺ T cells vs. T-bet⁺ CD8⁺ T cells, $P = 0.015$; T-bet⁺ CD4⁺ T cells vs. T-bet⁺ CD4⁺ T cells, $P = 2.06 \times 10^{-15}$, two-tailed Mann-Whitney U test). **d** Selection of ROIs in the TME of an ICI responder (ICI-12). T-bet⁺ PD-L1⁺

niches were identified using adjacent mIHC images (staining for T-bet, CD4, CD8, PD-1, PD-L1, pan-CK, and dapi). **e** Expression of MSS-PR-related genes (CXCL9, CXCL10, CCL3, CCL5, IFNG, GZMB, CXCR3, and IDO1) from the centers to the edges of T-bet⁺ PD-L1⁺ niches. Four niches were taken from an ICI responder (ICI-12), and another four were taken from an MSS-PR patient (GC-97). **f** Schematic graph of positive feedback loop between T-bet⁺ T cells and PD-L1⁺ tumor cells (Created in BioRender. Tang, Shiyang. (2025): <https://biorender.com/o50y390>; <https://biorender.com/d93b442>; <https://biorender.com/n49h689>; <https://biorender.com/c07s866>). * $P < 0.05$, ** $P < 0.01$, *** $P < 0.001$, **** $P < 0.0001$, ns is abbreviation for not significant.

highest mean value across samples was chosen for downstream analysis.

Single-cell RNA-seq data analysis

Raw counts files of scRNA sequencing of 26 primary tumor samples were downloaded from <https://www.ncbi.nlm.nih.gov/geo/> (accession number: GSE183904)⁵². As the original papers described, genes shared by less than three cells were filtered out; cells showing less than 500 or more than 6000 genes and cells with a mitochondrial RNA percentage of ≥ 20 were filtered out. We further filtered out samples with less than 1000 cells. Eventually, 26,571 genes of 119,878 cells remained for downstream analysis. ScRNA analysis was conducted by scanpy 1.8.1, according to the suggested protocol⁵³. Gene expressions were normalized by dividing the size factors of cells estimated by

calculateSumFactors function, followed by log transformation. Unsupervised clustering was conducted using Leiden algorithm (resolution = 1) on PC-reduced 10-dimensional features of 4000 highly-variable genes. Data was visualized using Uniform Manifold Approximation and Projection (UMAP). Cell types were manually annotated according to the expression pattern of the following markers: CD4⁺ T Cells (PTPRC⁺, CD3D⁺, IL7R⁺, CD8A⁻, FOXP⁻); CD8⁺ T Cells (PTPRC⁺, CD3D⁺, IL7R⁻, CD8A⁺); Natural Killer cells (PTPRC⁺, CD3D⁻, KLRD1⁺, NCAM1⁺); Treg Cells (PTPRC⁺, CD3D⁺, IL7R⁺, CD8A⁻, FOXP⁺); B Cells (PTPRC⁺, CD19⁺, CD79A⁺, SSR3^{low}, SSR4^{low}, CD83⁺); Plasma Cells (PTPRC^{low}, CD19^{low}, CD79A⁺, SSR3^{high}, SSR4^{high}, SDC1⁺); Monocytes/Macrophages (PTPRC⁺, CD14⁺, CD68⁺, CD83⁺, CD86⁺, CD163⁺); Dendritic Cells (PTPRC⁺, CD14⁺, CD16⁺, CD163⁺, CD74⁺, HLA-DR⁺); Mast Cells (PTPRC⁺, TPSB2⁺); Cancerous Epithelial Cells (EPCAM⁺, KRT8⁺, KRT18⁺, KRT19⁺, CLDN4^{high},

CLDN7^{high}, TFF2^{low}, MUC5AC^{low}); Normal Epithelial Cells (EPCAM⁺, KRT8⁺, KRT18⁺, KRT19⁺, CLDN4^{low}, CLDN7^{low}, TFF2^{high}, MUC5AC^{high}); Fibroblasts (COL1A1⁺, COL1A2⁺, COL3A1⁺); Vascular Endothelial Cells (PECAMI⁺, CD34⁺).

Raw counts of scRNA sequencing of tumor-infiltrating T cells were downloaded from <https://www.ncbi.nlm.nih.gov/geo/> (accession number: GSE156728)⁵⁴. Only tumor-infiltrating T cells in solid tumors were included for downstream analysis. We filtered out cells with fewer than 200 genes detected or >10% mitochondrial UMI counts and genes detected in ≤3 cells, as the original paper suggested. Gene expressions were normalized by dividing the size factors of cells estimated by calculateSumFactors function, followed by log transformation. T-bet⁺ CD4⁺ T cells or T-bet⁺ CD8⁺ T cells were defined as CD4⁺ T cells or CD8⁺ T cells with a normalized expression of TBX21 > 0. The R package “CellChat” was applied to construct and visualize intercellular communication networks. CellChat database for humans was used which includes 1939 validated interactions⁵⁵. Downstream analysis included inferring cell–cell communication probability (computeCommunProb and filterCommunication), and communication probability at CXCL signaling pathway.

Whole exon sequencing data preprocessing

Original fasta files of PRJEB25780 cohort were downloaded from <https://www.ebi.ac.uk/>. WES reads were aligned to the reference human genome GRCh38 using BWA-MEM, followed by indel realignment and base recalibration using the Genome Analysis Toolkit (GATK, version 4.2.4.1) to generate analysis-ready BAM files⁵⁶.

Immune infiltration estimation

The fractions of 22 immune cells were estimated using CibersortX (absolute mode) run for 1000 permutations for both RNA-seq and microarray data⁵⁷. Samples with a *P* value < 0.05 were included in downstream analysis. QuanTiseq was applied to calculate the fraction of tumor-infiltrating T cells, using aggregates of CD4⁺ T cells, CD8⁺ T cells, and Treg⁵⁸. Fractions of T-bet⁺ CD8⁺ T cells in PRJEB25780 and PRJEB40416 cohorts were inferred by CibersortX using a GC-specific signature matrix built on annotated scRNA-seq data (Supplementary Data File 6).

Positive Unlabeled Learning (PUL)

Two separate positive unlabeled machine learning models were constructed due to the substantial difference in RNA-seq and microarray data structure.

Identification of positive labeled samples and unlabeled samples

Positive samples in TCGA-STAD cohort were defined as MSI-H patients whose TMB is at the top 20% of all patients and whose fraction of tumor-infiltrating T cells is also at the top 20% estimated by QuanTiseq. Positive samples in ACRG were defined as MSI-H patients whose fraction of tumor-infiltrating T cells is at the top 20% of all patients, as estimated by QuanTiseq, due to the absence of TMB information. All MSS patients in TCGA-STAD, ACRG, and PRJEB25780 were defined as unlabeled samples, regardless of their TMB, T cell infiltration, or clinical outcomes.

Construction of immunologic features

4872 immunologic signature gene sets (ImmuneSigDB subset of C7) were downloaded from <https://www.gsea-msigdb.org/gsea/msigdb/>. Signature gene sets of 28 immune cell types were retrieved from published data⁵⁹. The original immunologic features were constructed using single-sample GSEA running on the combined 5000 gene sets⁶⁰. High-variance features were selected using sklearn.feature_selection function, setting variance threshold at 5e-04. Principal Component analysis was conducted on those selected high-variance features to comprise a finalized 5-dimensional immunologic feature.

Construction of training and validation PUL models

Training dataset (TCGA or ACRG data), validation dataset (MSS patients in PRJEB25780), and an extended validation dataset (MSI-H patients in PRJEB25780 and PRJEB40416) were included in the study. The training PUL models predict the PUL scores of MSS patients TCGA-STAD data (RNA-seq data) and MSS patients in ACRG data (microarray data), respectively. Then the validation PUL models were constructed using positive and unlabeled samples in TCGA-STAD data plus one sample from the validation/extended validation dataset, the PUL score of the respective sample of the validation datasets was predicted one at a time. After iteration of all samples in the validation/extended validation dataset, their PUL scores were used to assess their specificity and sensitivity for predicting ICI responses.

Implementation of positive unlabeled learning

A bagging support vector machine positive unlabeled learning model is constructed as originally described by Mordelet et al. and implemented using the python package pulearn <https://pulearn.github.io/pulearn/doc/pulearn/>²⁸. A PUL score of an unlabeled sample was calculated as the mean value of 1000 permutations of predictions (positive as 1, negative as 0).

Patients with a PUL score ≥ 0.953 were considered potential responders in MSS patients (MSS-PRs).

Somatic Mutation Calculation

VarScan2 calculated mutation data of TCGA-STAD cohort were downloaded from GDC data portal (<https://portal.gdc.cancer.gov/>). For PRJEB25780 and PRJEB40416 cohorts, a panel of normals (PON) was first created using all adjacent normal samples in PRJEB25780 cohort by Mutect2 tumor-only mode. Then somatic mutations of tumor samples were calculated using Mutect2 on tumor-normal match mode (using tumor bam, matched normal bam, and PON as inputs). Only moderate or high-impact mutations were included for downstream analysis.

Copy number variation (CNV) analysis

Original CNV segment data of TCGA-STAD cohort were downloaded from GDC data portal (<https://portal.gdc.cancer.gov/>). CNV segments of MSS-PRs or MSS-NRs were aggregated into two separate segment files to infer CNVs on a subgroup level. GISTIC 2.0 analysis was conducted on the public server provided by GenePattern (<https://www.genepattern.org/>), using parameters suggested by GDC documentation (https://docs.gdc.cancer.gov/Data/Bioinformatics_Pipelines/CNV_Pipeline/)⁶¹. A *q* value ≤ 0.05 was considered significant for CN deletion and amplification.

Differential expression gene (DEG) analysis

Differential expression analysis of RNA-seq data was conducted on raw counts of respective datasets using ‘DESeq2’⁶². Differential expression analysis of microarray data was conducted on log2 normalized data using ‘Limma’⁶³. *P* values were adjusted using Benjamini-Hochberg methods; an adjusted *P* value < 0.05 was considered significant. Up-regulated genes in MSS-PR were defined as DEGs with significant *P* values and positive log fold changes in both TCGA-STAD and ACRG cohorts. Down-regulated genes in MSS-PR were defined as DEGs with significant *P* values and negative log fold changes in both TCGA-STAD and ACRG cohorts.

Multiplex immunohistochemistry (mIHC)

Opal 7-Color Manual IHC Kit (Akoya Biosciences, NEL811001KT) was used for mIHC. 4 μm-thick FFPE sections were dewaxed and rehydrated. In the first round of antigen retrieval, slides were immersed in preheated EDTA solution (PH = 8.0, 95 °C) and heated with a microvan for 15 min at low power, then cooled to room temperature (RT), washed with TBST/0.5% Tween (3 times, 5 min). Slides were washed

and blocked with a blocking buffer for 10 min. Primary antibody, CD4⁺ (MXB Biotechnologies, MAB-0251, prediluted), was incubated at RT for 1 h. Slides were washed and incubated with an HRP-conjugated secondary antibody (1:1000) at RT for 10 min. Opal 650 fluorophore (1:200) was applied for 10 min after washes. The procedure described above was repeated five more times using the following antibody-fluorophore combinations: PD-1 (Cell Signaling Technology, 86163, 1:100) with opal 620 fluorophore (1:100), CD8⁺ (MXB Biotechnologies, MAB-0021, prediluted) with opal 540 fluorophore (1:300), pan-CK (MXB Biotechnologies, kit-0009, prediluted) with opal 690 fluorophore (1:60), PD-L1 (Cell Signaling Technology, 13684, 1:200) with opal 570 fluorophore (1:150) and T-bet (Abcam, ab154200, 1:100) with opal 520 fluorophore (1:100). To visualize the co-localization of CXCR3 and T-bet, PD-L1 primary antibody was replaced with CXCR3 primary antibody (R&D, MAB160, 10 µg/ml), with other conditions unchanged.

Analysis of mIHC images

Nice or more images were acquired from each slide at 20× using a Mantra 2 Quantitative Pathology Workstation (Akoya Biosciences). For slides with a distinct tumor-normal interface, images of adjacent normal tissues (N), margins at the tumor-normal interface (M), tumor edges near the interface (E), and tumor cores (C) were acquired too. Acquired images were analyzed using inForm 2.3.0 (Akoya Biosciences), following tissue segmentation, cell segmentation, and cell phenotyping. A supervised machine learning model was trained on pre-defined tumor compartments, stroma compartments, and blank areas based on the expression patterns of pan-CK. Cell segmentation of tumor and stroma compartments were trained separately, due to the substantial difference in cellular morphology, based on the counterstain DAPI. Every individual cell in the tumor and stroma compartments was phenotyped using the following cutoff intensities: T-bet (opal 520) ≥ 2, CD8⁺ (opal 540) ≥ 2, PD-L1 (opal 570) ≥ 2, PD-1 (opal 620) ≥ 2, CD4⁺ (opal 650) ≥ 2, pan-CK (opal 690) ≥ 2.

Quantification of neighboring cells of T-bet⁺/T-bet⁻ T cells

To evaluate whether T-bet⁺ T cells can up-regulate PD-L1 on neighboring cells, coordination information of 132,241 T cells in the GC cohort was retrieved. The neighboring cells of a specific T cell were defined as any cells within a 50 µm radius. The percentage of PD-L1⁺ neighboring cells was calculated for each T cell.

Spatial transcriptomic profiling

FFPE samples of ICI-12 (partial response, MSI-H) and GC-97 (potential responder, MSS) were firstly stained with mIHC protocol described above to identify the locations of T-bet⁺PD-L1⁺ niches. Four niches were identified from each slide. Then adjacent FFPE slides were processed following the GeoMx[®] DSP slide preparation user manual. Slides were baked in an oven at 60 °C for at least 3 h to retrieve antigens. Proteinase K was added to digest the proteins after deparaffination and hydration. The slides were incubated with WTA probe mix overnight. On the second day, the slides were stained with PD-L1 (OriGene, CF809809), CD45 (CST, 13917), PanCK (Novus, NBP2-33200AF532), and Syto13 (ThermoFisher, S7575) for 2 h. Three concentric circles on each T-bet⁺ - PD-L1 niche were chosen as regions of interest (ROIs). For each ROI, areas of interest (AOIs) were further divided into immune cells and cancer cells, based on CD45 and PanCK protein expression. Each Oligos from ROIs were collected by UV-cleavage. PCR reactions were purified. Libraries were paired-end sequenced. Raw counts of all ROIs were obtained by GeoMx[®] DSP data analysis software. Reads were further normalized using Q3 normalization approach with background subtraction.

T cells culture and expansion

Human PBMCs from healthy donors were isolated by centrifugation 400 g for 30 min in Ficoll solution (Tbd science, LTS1077). Non-CD3⁺

cells or non-CD8⁺ cells in PBMCs were depleted by incubating with the biotin antibody cocktail, followed by incubation with magnetic Streptavidin Nanobeads (Biolegend, 480022, 480012). Untouched CD3⁺ or CD8⁺ cells were collected using a magnetic separator (StemCell Technologies, 18000). CD3⁺ cells or CD8⁺ cells were then washed and resuspended with human lymphocyte media (Takara, GT-T551) + 10% FBS (Gibco, 10099) at 1 × 10⁶/ml concentration. 1 ng/ml CD3 antibody (BD Biosciences, 566685) and 5 ng/ml CD28 antibody (BD Biosciences, 555725) were coated on non-TC treated 12-well plate (Nest, 712011) at 4 °C overnight. T cells were activated using CD3/CD28 antibodies-coated plate for 48 h. After activation, IL-2 (100 IU/ml, Peprotech, 200-02) was added to the media to expand T cells rapidly. Fresh IL-2 was added daily, and cell densities were maintained at 0.5–2 × 10⁶/ml throughout the in-vitro culture process. T cells were reactivated every 7 days using CD3/CD28 antibodies coated plate, and dead cells were removed using Dead Cell Removal Kit, following the manufacturer's instructions (Miltenyi Biotec, 130-090-101).

Inducing T-bet expression in T cells

The expression of T-bet is up-regulated by IFN-γ and IL-12 stimulation in T cells^{33–35}. 72 h after CD3/CD28 antibodies withdrawal, IL-12 (50 ng/ml, Peprotech, 200-12H) was added to the medium to induce T-bet^{high} CD3⁺ T cells (or T-bet^{high} CD8⁺ T cells), and the same volume of PBS was added to maintain low expression of T-bet in the control group. Fresh IL-12 was added every day for at least two successive days. CD3/CD28 antibodies were depleted in both groups throughout the process. Up-regulation of T-bet and downstream cytokines in T cells was confirmed by intracellular flow cytometry.

Tumor-bearing humanized mouse model

Four to six-week-old female NYG (Prkdc^{-/-}IL2RG^{-/-}NOD, stock number: 091202) mice were purchased from Liaoning Changsheng Biotechnology and housed under pathogen-free conditions. 5 × 10⁶ PBMCs of five different healthy donors were intravenously injected into mice at day 0. After the reconstruction of mice's immune system, 5 × 10⁶ HGC-27 cells were subcutaneously implanted into the right flank of mice on day 5. Mice were randomly assigned to T-bet^{high} group and T-bet^{low} group on day 8. On day 8 and day 10, 1 × 10⁷ T-bet^{high} or T-bet^{low} CD3⁺ T cells derived from the same healthy donor (as the PBMCs donor) were injected through tail veins. Tumor width and diameter were measured by an independent investigator blinded to treatment conditions every 2 days. Tumor volume was calculated as 1/2 × (Length × Width²). The maximal tumor size permitted in this study is 20 mm at largest diameter. All animal experiment protocols were approved by the Research Ethics Committee of China Medical University (#CMUXN2021712).

Immune-ignorant tumor-bearing humanized mouse model

HGC-27 cells were subcutaneously implanted into the right flank of multiple NYG mice. Immune-ignorant tumors were harvested when their lengths exceeded 1 cm. Tumors were evenly cut into 20 mm³ grafts and were subcutaneously transplanted into the right flank of humanized mice engineered as described above. On day 5 and day 7 after transplantation, 5 × 10⁶ T-bet^{high} or T-bet^{low} CD8⁺ T cells derived from the same healthy donor (as the PBMCs donor) were injected through tail veins. Every 2 days after transplantation, anti-PD-1 (200 µg/injection, Toripalimab, Junshi Pharma) or human IgG4 isotype control (50 µg/injection, Sigma-Aldrich, 14640) was administered through tail vein. Tumor width and diameter were measured by an independent investigator blinded to treatment conditions every 2 days. The maximal tumor size permitted in this study is 20 mm at largest diameter. All animal experiment protocols were approved by the Research Ethics Committee of China Medical University (#CMUXN2021712).

T cells migration assay

CD8⁺ T Cells from 5 different healthy donors were isolated and activated as described above. T-bet expression was induced using IL-12 (50 ng/ml, Peprotech, 200-12H) on two successive days. A total of 1×10^6 T-bet^{high} CD8⁺ T cells or T-bet^{low} CD8⁺ T cells were seeded in 0.4-μm pore size membrane upper chambers of transwell plate with 1×10^5 pre-seeded HGC-27 cells in the lower chambers. IFN-γ neutralizing antibody (0.5 μg/ml, Proteintech, 69007-1-Ig) or AMG487 (1 μM, Selleckchem, S8682) were added in the lower chambers as needed followed by another 16 h incubation in RPMI 1640 + 10% FBS medium in a 37 °C incubator for. Migrated cells were fix with 95% alcohol for 1 min. Wright-Giemsa Quick Stain Kit (Phygene, PH1793) was used for cell staining. Three fields of view were randomly selected under a 200 × high power microscope, the number of migrated cells was defined as the cells in the lower surface of the upper chamber.

Isolation of tumor-infiltrating immune cells

Tumors of GC patients and CDX mice models were cut into small pieces with sterile scissors in HBBS containing calcium and magnesium (Solarbio, H1025). Tissue was dissociated in 200 U/ml Collagenase Type IV (Gibco, 17104019), 3 mM CaCl₂ (Solarbio, C7250), 0.01 mg/mL DNase I (Solarbio, D8071), and 0.025 mg/mL Hyaluronidase (Solarbio, H8030) using GentleMACS C tubes on the GentleMACS Dissociator (Miltenyi Biotec, 130-093-235), followed by incubation at 37 °C for 1 h. The resulting cell suspension was passed through a 70-μm filter (MACS SmartStrainers, 5201110409) and pelleted by centrifugation at 350 g for 5 minutes. Red blood cells were removed by incubating in RBC lysis buffer (Biolegend, 420301) for 10 min at room temperature. Cells were washed twice and resuspended in calcium/magnesium-free HBBS (Solarbio, H1040). CD45⁺ cells were then isolated using CD45⁺ positive beads (StemCell Technologies, 100-0107) with a magnetic separator.

Multi-color flow cytometry

Single-cell suspensions were stained with 5 μg/ml human Fc receptor blocking solution (Biolegend, 422302) for 5 min at 4 °C. The cells were stained with fluorochrome-conjugated antibodies cocktail for 40 minutes at 4 °C. Multi-color flow cytometry was performed using a Spectral Analyzer (Sony, SA3800), and the data were analyzed using FlowJo V10.4 software. For intracellular staining of T-bet, surface-stained cells were fixed and permeabilized using Transcription Factor Buffer Set (BD Biosciences, 562574) according to the manufacturer's instructions. For intracellular staining of cytokines, PMA (Sigma-Aldrich, P8139) and ionomycin (Sigma-Aldrich, I3909) were added for 12 h followed by brefeldin A (Biolegend, 420601) for another 4 h to enhance intracellular staining signals before proceeding to cell surface staining.

Statistics & reproducibility

Statistical significance was determined using two-tailed Mann–Whitney *U* test for comparison between 2 groups unless otherwise indicated in the figure legends. Chi-square test was used to compare gene mutation frequency between MSS-PRs and MSS-NRs. Kaplan–Meier Analysis of overall survival in the GC cohort was conducted by R package ‘survival’ (version 3.5). To compare tumor sizes between 2 groups, data collected at different time points were included for two-way ANOVA analysis, with time and interference as two independent variables. The Benjamini–Hochberg correction method was applied to decrease false discovery rates for multiple comparisons. *P* values lower than 0.05 were considered statistically significant (**P* < 0.05, ***P* < 0.01, ****P* < 0.001, *****P* < 0.0001). All statistical analyzes were performed using R 4.1.1 or SciPy 1.8.1 (Python 3.9.7). No statistical method was used to pre-determine sample size. No data were excluded from the analyzes. For mice studies, randomization was applied before assigning treatment groups, and tumor volumes were measured by investigators blinded to treatment conditions.

Reporting summary

Further information on research design is available in the Nature Portfolio Reporting Summary linked to this article.

Data availability

Original data to construct the PUL model was available in Supplementary Data File 1; Original data of mIHC images were available in Supplementary Data File 5; Clinical information of patients in the GC cohort and the GC-ICI cohort was available in the extended data tables. Spatial RNA-seq data generated in this study have been deposited in the Genome Sequence Archive for Human (GSA-Human) database under accession code [HRA005361](https://ngdc.cncb.ac.cn/bioproject/browse/PRJCA019016) (<https://ngdc.cncb.ac.cn/bioproject/browse/PRJCA019016>). The Data is under restricted access for privacy reason. Access will be granted for academic use only. Access can be granted by request from the corresponding author (Yunpeng Liu, ypliu@cmu.edu.cn). The expected timeframe for processing access requests is 2 weeks. Bulk RNA-seq data of ACRG cohort (<https://www.ncbi.nlm.nih.gov/geo/>, accession code: [GSE62254](https://www.ncbi.nlm.nih.gov/geo/query/acc.cgi?acc=GSE62254) (<https://www.ncbi.nlm.nih.gov/geo/query/acc.cgi?acc=GSE62254>); Bulk RNA-seq data and mutational data of TCGA-STAD cohort (<https://portal.gdc.cancer.gov/>); ScRNA-seq data of GCs (<https://www.ncbi.nlm.nih.gov/geo/>, accession code: [GSE183904](https://www.ncbi.nlm.nih.gov/geo/query/acc.cgi?acc=GSE183904) (<https://www.ncbi.nlm.nih.gov/geo/query/acc.cgi?acc=GSE183904>); ScRNA-seq data of tumor-infiltrating T cells (<https://www.ncbi.nlm.nih.gov/geo/>, accession code: [GSE156728](https://www.ncbi.nlm.nih.gov/geo/query/acc.cgi?acc=GSE156728) (<https://www.ncbi.nlm.nih.gov/geo/query/acc.cgi?acc=GSE156728>); WES and bulk RNA-seq data of PRJEB25780 and PRJEB40416 cohorts (<https://www.ebi.ac.uk/>, accession codes: [PRJEB25780](https://www.ebi.ac.uk/ena/browser/view/PRJEB25780) (<https://www.ebi.ac.uk/ena/browser/view/PRJEB25780>), [PRJEB40416](https://www.ebi.ac.uk/ena/browser/view/PRJEB40416) (<https://www.ebi.ac.uk/ena/browser/view/PRJEB40416>). Source data are provided with this paper.

Code availability

Codes used in the study can be accessed at https://github.com/Tsy97/TbetCD8_paper.git⁶⁴.

References

- Sung, H. et al. Global cancer statistics 2020: GLOBOCAN estimates of incidence and mortality worldwide for 36 cancers in 185 countries. *CA Cancer J. Clin.* **71**, 209–249 (2021).
- Bouche, O. et al. Randomized multicenter phase II trial of a biweekly regimen of fluorouracil and leucovorin (LV5FU2), LV5FU2 plus cisplatin, or LV5FU2 plus irinotecan in patients with previously untreated metastatic gastric cancer: a federation francophone de cancerologie digestive group study–FFCD 9803. *J. Clin. Oncol.* **22**, 4319–4328 (2004).
- Al-Batran, S. E. et al. Phase III trial in metastatic gastroesophageal adenocarcinoma with fluorouracil, leucovorin plus either oxaliplatin or cisplatin: a study of the arbeitsgemeinschaft internistische onkologie. *J. Clin. Oncol.* **26**, 1435–1442 (2008).
- Kang, Y. K. et al. Capecitabine/cisplatin versus 5-fluorouracil/cisplatin as first-line therapy in patients with advanced gastric cancer: a randomised phase III noninferiority trial. *Ann. Oncol.* **20**, 666–673 (2009).
- Enzinger, P. C. et al. CALGB 80403 (Alliance)/E1206: a randomized phase II study of three chemotherapy regimens plus cetuximab in metastatic esophageal and gastroesophageal junction cancers. *J. Clin. Oncol.* **34**, 2736–2742 (2016).
- Brahmer, J. R. et al. Safety and activity of anti-PD-L1 antibody in patients with advanced cancer. *N. Engl. J. Med.* **366**, 2455–2465 (2012).
- Topalian, S. L. et al. Safety, activity, and immune correlates of anti-PD-1 antibody in cancer. *N. Engl. J. Med.* **366**, 2443–2454 (2012).
- Chao, J. et al. Assessment of pembrolizumab therapy for the treatment of microsatellite instability-high gastric or gastro-esophageal junction cancer among patients in the KEYNOTE-059,

- KEYNOTE-061, and KEYNOTE-062 Clinical Trials. *JAMA Oncol.* **7**, 895–902 (2021).
9. Shitara, K. et al. Efficacy and safety of pembrolizumab or pembrolizumab plus chemotherapy vs chemotherapy alone for patients with first-line, advanced gastric cancer: the KEYNOTE-062 phase 3 randomized clinical trial. *JAMA Oncol.* **6**, 1571–1580 (2020).
 10. Marabelle, A. et al. Efficacy of pembrolizumab in patients with noncolorectal high microsatellite instability/mismatch repair-deficient cancer: results from the phase II KEYNOTE-158 Study. *J. Clin. Oncol.* **38**, 1–10 (2020).
 11. Fuchs, C. S. et al. Safety and efficacy of pembrolizumab monotherapy in patients with previously treated advanced gastric and gastroesophageal junction cancer: phase 2 clinical KEYNOTE-059 Trial. *JAMA Oncol.* **4**, e180013 (2018).
 12. Kang, B. W. & Chau, I. Current status and future potential of predictive biomarkers for immune checkpoint inhibitors in gastric cancer. *ESMO Open* **5**, e000791 (2020).
 13. Lee, V., Murphy, A., Le, D. T. & Diaz, L. A. Jr Mismatch repair deficiency and response to immune checkpoint blockade. *Oncologist* **21**, 1200–1211 (2016).
 14. Kim, J. Y. et al. Microsatellite instability status in gastric cancer: a reappraisal of its clinical significance and relationship with mucin phenotypes. *Korean J. Pathol.* **47**, 28–35 (2013).
 15. Lee, K. W. et al. Association of tumor mutational burden with efficacy of pembrolizumab +/- chemotherapy as first-line therapy for gastric cancer in the phase III KEYNOTE-062 Study. *Clin. Cancer Res.* **28**, 3489–3498 (2022).
 16. Kim, S. T. et al. Comprehensive molecular characterization of clinical responses to PD-1 inhibition in metastatic gastric cancer. *Nat. Med.* **24**, 1449–1458 (2018).
 17. Wang, F. et al. Safety, efficacy and tumor mutational burden as a biomarker of overall survival benefit in chemo-refractory gastric cancer treated with toripalimab, a PD-1 antibody in phase Ib/II clinical trial NCT02915432. *Ann. Oncol.* **30**, 1479–1486 (2019).
 18. Kubota, Y. et al. The impact of molecular subtype on efficacy of chemotherapy and checkpoint inhibition in advanced gastric cancer. *Clin. Cancer Res.* **26**, 3784–3790 (2020).
 19. Qiu, M. Z. et al. Observational cohort study of clinical outcome in Epstein-Barr virus associated gastric cancer patients. *Ther. Adv. Med. Oncol.* **12**, 1758835920937434 (2020).
 20. Binnewies, M. et al. Understanding the tumor immune microenvironment (TIME) for effective therapy. *Nat. Med.* **24**, 541–550 (2018).
 21. Sun, C. et al. Spatially resolved multi-omics highlights cell-specific metabolic remodeling and interactions in gastric cancer. *Nat. Commun.* **14**, 2692 (2023).
 22. Chen, Y. et al. Predicting response to immunotherapy in gastric cancer via multi-dimensional analyses of the tumour immune microenvironment. *Nat. Commun.* **13**, 4851 (2022).
 23. Sun, K. et al. scRNA-seq of gastric tumor shows complex inter-cellular interaction with an alternative T cell exhaustion trajectory. *Nat. Commun.* **13**, 4943 (2022).
 24. Cristescu, R. et al. Molecular analysis of gastric cancer identifies subtypes associated with distinct clinical outcomes. *Nat. Med.* **21**, 449–456 (2015).
 25. Verreck, F. A. et al. Human IL-23-producing type 1 macrophages promote but IL-10-producing type 2 macrophages subvert immunity to (myco)bacteria. *Proc. Natl Acad. Sci. USA* **101**, 4560–4565 (2004).
 26. Wei, S. C., Duffy, C. R. & Allison, J. P. Fundamental mechanisms of immune checkpoint blockade therapy. *Cancer Discov.* **8**, 1069–1086 (2018).
 27. Denis, F., Gilleron, R. & Letouzey, F. Learning from positive and unlabeled examples. *Theor. Computer Sci.* **348**, 70–83 (2005).
 28. Mordelet, F. & Vert, J. P. A bagging SVM to learn from positive and unlabeled examples. *Pattern Recognit. Lett.* **37**, 201–209 (2014).
 29. Kwon, M. et al. Determinants of response and intrinsic resistance to PD-1 blockade in microsatellite instability-high. *Gastric Cancer Cancer Discov.* **11**, 2168–2185 (2021).
 30. Dong, M. et al. Expression and prognostic roles of PIK3CA, JAK2, PD-L1, and PD-L2 in Epstein-Barr virus-associated gastric carcinoma. *Hum. Pathol.* **53**, 25–34 (2016).
 31. Morales-Sanchez, A. & Fuentes-Panana, E. M. Epstein-barr virus-associated gastric cancer and potential mechanisms of oncogenesis. *Curr. Cancer Drug Targets* **17**, 534–554 (2017).
 32. Tokunaga, R. et al. CXCL9, CXCL10, CXCL11/CXCR3 axis for immune activation - a target for novel cancer therapy. *Cancer Treat. Rev.* **63**, 40–47 (2018).
 33. Lighvani, A. A. et al. T-bet is rapidly induced by interferon-gamma in lymphoid and myeloid cells. *Proc. Natl Acad. Sci. USA* **98**, 15137–15142 (2001).
 34. Afkarian, M. et al. T-bet is a STAT1-induced regulator of IL-12R expression in naive CD4 + T cells. *Nat. Immunol.* **3**, 549–557 (2002).
 35. Takemoto, N., Intlekofer, A. M., Northrup, J. T., Wherry, E. J. & Reiner, S. L. Cutting Edge: IL-12 inversely regulates T-bet and eomesodermin expression during pathogen-induced CD8 + T cell differentiation. *J. Immunol.* **177**, 7515–7519 (2006).
 36. Chow, M. T. et al. Intratumoral activity of the CXCR3 chemokine system is required for the efficacy of anti-PD-1 therapy. *Immunity* **50**, 1498–1512 e1495 (2019).
 37. Pelka, K. et al. Spatially organized multicellular immune hubs in human colorectal cancer. *Cell* **184**, 4734–4752 e4720 (2021).
 38. Cruz-Guilloty, F. et al. Runx3 and T-box proteins cooperate to establish the transcriptional program of effector CTLs. *J. Exp. Med.* **206**, 51–59 (2009).
 39. Lazarevic, V., Glimcher, L. H. & Lord, G. M. T-bet: a bridge between innate and adaptive immunity. *Nat. Rev. Immunol.* **13**, 777–789 (2013).
 40. Jenner, R. G. et al. The transcription factors T-bet and GATA-3 control alternative pathways of T-cell differentiation through a shared set of target genes. *Proc. Natl Acad. Sci. USA* **106**, 17876–17881 (2009).
 41. Gao, J. et al. Loss of IFN-gamma pathway genes in tumor cells as a mechanism of resistance to anti-CTLA-4. *Ther. Cell* **167**, 397–404 e399 (2016).
 42. Zaretsky, J. M. et al. Mutations associated with acquired resistance to PD-1 blockade in melanoma. *N. Engl. J. Med.* **375**, 819–829 (2016).
 43. Lu, C. et al. DNA sensing in mismatch repair-deficient tumor cells is essential for anti-tumor immunity. *Cancer Cell* **39**, 96–108 e106 (2021).
 44. Lord, G. M. et al. T-bet is required for optimal proinflammatory CD4 + T-cell trafficking. *Blood* **106**, 3432–3439 (2005).
 45. Doroshov, D. B. et al. PD-L1 as a biomarker of response to immune-checkpoint inhibitors. *Nat. Rev. Clin. Oncol.* **18**, 345–362 (2021).
 46. Herbst, R. S. et al. Predictive correlates of response to the anti-PD-L1 antibody MPDL3280A in cancer patients. *Nature* **515**, 563–567 (2014).
 47. Yong, C. S. M. et al. CAR T-cell therapy of solid tumors. *Immunol. Cell Biol.* **95**, 356–363 (2017).
 48. Li, B. & Dewey, C. N. RSEM: accurate transcript quantification from RNA-Seq data with or without a reference genome. *BMC Bioinform.* **12**, 323 (2011).
 49. Dobin, A. et al. STAR: ultrafast universal RNA-seq aligner. *Bioinformatics* **29**, 15–21 (2013).
 50. Liu, J. et al. An integrated TCGA pan-cancer clinical data resource to drive high-quality survival outcome analytics. *Cell* **173**, 400–416.e411 (2018).
 51. Zhang, Y., Parmigiani, G. & Johnson, W. E. ComBat-seq: batch effect adjustment for RNA-seq count data. *NAR Genom. Bioinform* **2**, lqaa078 (2020).
 52. Kumar, V. et al. Single-cell atlas of lineage states, tumor microenvironment, and subtype-specific expression programs in gastric cancer. *Cancer Discov.* **12**, 670–691 (2022).

53. Wolf, F. A., Angerer, P. & Theis, F. J. SCANPY: large-scale single-cell gene expression data analysis. *Genome Biol.* **19**, 15 (2018).
54. Zheng, L. et al. Pan-cancer single-cell landscape of tumor-infiltrating T cells. *Science* **374**, abe6474 (2021).
55. Jin, S. et al. Inference and analysis of cell-cell communication using CellChat. *Nat. Commun.* **12**, 1088 (2021).
56. McKenna, A. et al. The genome analysis toolkit: a mapreduce framework for analyzing next-generation DNA sequencing data. *Genome Res* **20**, 1297–1303 (2010).
57. Newman, A. M. et al. Determining cell type abundance and expression from bulk tissues with digital cytometry. *Nat. Biotechnol.* **37**, 773–782 (2019).
58. Finotello, F. et al. Molecular and pharmacological modulators of the tumor immune contexture revealed by deconvolution of RNA-seq data. *Genome Med* **11**, 34 (2019).
59. Charoentong, P. et al. Pan-cancer immunogenomic analyses reveal genotype-immunophenotype relationships and predictors of response to checkpoint blockade. *Cell Rep.* **18**, 248–262 (2017).
60. Hanzelmann, S., Castelo, R. & Guinney, J. GSVA: gene set variation analysis for microarray and RNA-seq data. *BMC Bioinforma.* **14**, 7 (2013).
61. Mermel, C. H. et al. GISTIC2.0 facilitates sensitive and confident localization of the targets of focal somatic copy-number alteration in human cancers. *Genome Biol.* **12**, R41 (2011).
62. Love, M. I., Huber, W. & Anders, S. Moderated estimation of fold change and dispersion for RNA-seq data with DESeq2. *Genome Biol.* **15**, 550 (2014).
63. Ritchie, M. E. et al. limma powers differential expression analyses for RNA-sequencing and microarray studies. *Nucleic Acids Res* **43**, e47 (2015).
64. Tang, S. et al. T-bet+CD8+ T cells govern anti-PD-1 responses in microsatellite-stable gastric cancers. *Zenodo* (2025).

Acknowledgements

We thank Shenyang Gernster Biotechnology Co., Ltd for assisting in the construction of tumor-bearing mice models. We thank Ms. Miao Li from Liaoning Chinese medicine school for assisting with multiplex immunohistochemistry. This work was supported by The Noncommunicable Chronic Diseases-National Science and Technology Major Project (No. 2023ZD0501500, Z.W.), The National Key Research and Development Program of China (No. 2017YFC1308900, Y.L.), National Natural Science Foundation of China (No. 81972751, Y.L.; No. 32170791, X.C.; No. 81972331, X.Q.), Technological Special Project of Liaoning Province of China (2019020176-JH1/103, Y.L.), Research Project of Education Department of Liaoning Province (No. ZD2020001, J.W.). The authors would like to acknowledge the Key Laboratory of Precision Diagnosis and Treatment of Gastrointestinal Tumors (China Medical University), Ministry of Education, and Clinical Cancer Research Center of Shenyang (China Medical University) for providing the space and equipment for conducting the experiments.

Author contributions

Conceptualization: S.T., X.C., Y.L. Methodology: S.T., X.C., J.W., L.C., D.L. Validation: C.L., X.H. Formal analysis: S.T., X.C. Investigation: S.T., X.C. Resources: Y.L., Z.W., X.Q., X.C. Data Curation: S.T., X.C., X.Z., C.L., X.H. Writing - Original Draft: S.T. Writing - Review & Editing: X.C., Y.L., Z.W., X.Q. Visualization: S.T., J.G., B.Y. Supervision: Y.L., Z.W., X.Q. Project administration: Y.L., Z.W., X.Q., K.H., X.Z., Funding acquisition: Y.L., X.Q., Z.W., X.C., J.W.

Competing interests

X.C., X.Q., Y.L., and S.T. declare a pending patent (P012510580) regarding T-bet+ CD8+ T cells as a therapeutic biomarker in GI cancers. The remaining authors declare no competing interests.

Additional information

Supplementary information The online version contains supplementary material available at <https://doi.org/10.1038/s41467-025-58958-1>.

Correspondence and requests for materials should be addressed to Xiujian Qu, Zhenning Wang or Yunpeng Liu.

Peer review information *Nature Communications* thanks the anonymous reviewer(s) for their contribution to the peer review of this work. A peer review file is available.

Reprints and permissions information is available at <http://www.nature.com/reprints>

Publisher's note Springer Nature remains neutral with regard to jurisdictional claims in published maps and institutional affiliations.

Open Access This article is licensed under a Creative Commons Attribution-NonCommercial-NoDerivatives 4.0 International License, which permits any non-commercial use, sharing, distribution and reproduction in any medium or format, as long as you give appropriate credit to the original author(s) and the source, provide a link to the Creative Commons licence, and indicate if you modified the licensed material. You do not have permission under this licence to share adapted material derived from this article or parts of it. The images or other third party material in this article are included in the article's Creative Commons licence, unless indicated otherwise in a credit line to the material. If material is not included in the article's Creative Commons licence and your intended use is not permitted by statutory regulation or exceeds the permitted use, you will need to obtain permission directly from the copyright holder. To view a copy of this licence, visit <http://creativecommons.org/licenses/by-nc-nd/4.0/>.

© The Author(s) 2025